Max-Planck-Institut
für Meteorologie

MAX PLANCK
GESELLSCHAFT

International Max Planck Research School
on Earth System Modelling

A split-explicit time-stepping scheme for ICON-Ocean

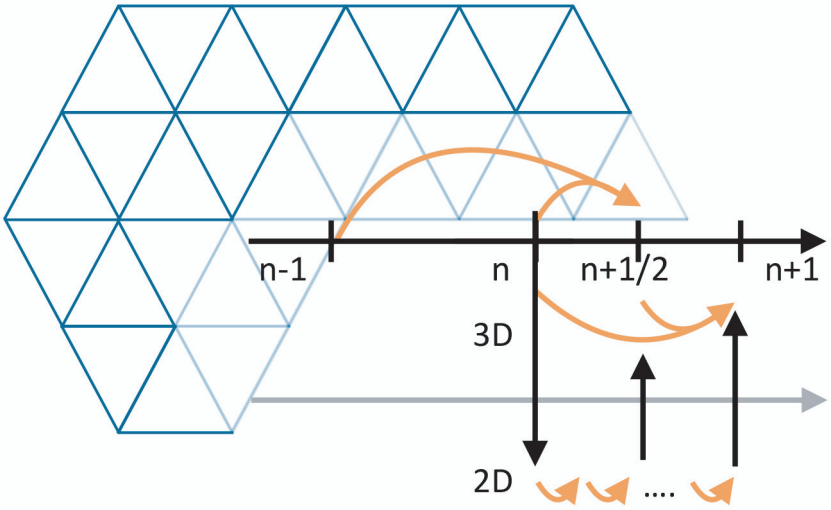

Lukas Krönert

Hamburg 2021

Berichte zur Erdsystemforschung
Reports on Earth System Science

242
2021

Hinweis

Die Berichte zur Erdsystemforschung werden vom Max-Planck-Institut für Meteorologie in Hamburg in unregelmäßiger Abfolge herausgegeben.

Sie enthalten wissenschaftliche und technische Beiträge, inklusive Dissertationen.

Die Beiträge geben nicht notwendigerweise die Auffassung des Instituts wieder.

Die "Berichte zur Erdsystemforschung" führen die vorherigen Reihen "Reports" und "Examensarbeiten" weiter.

Notice

The Reports on Earth System Science are published by the Max Planck Institute for Meteorology in Hamburg. They appear in irregular intervals.

They contain scientific and technical contributions, including Ph. D. theses.

The Reports do not necessarily reflect the opinion of the Institute.

The "Reports on Earth System Science" continue the former "Reports" and "Examensarbeiten" of the Max Planck Institute.

Anschrift / Address

Max-Planck-Institut für Meteorologie
Bundesstrasse 53
20146 Hamburg
Deutschland

Tel./Phone: +49 (0)40 4 11 73 - 0
Fax: +49 (0)40 4 11 73 - 298

name.surname@mpimet.mpg.de
www.mpimet.mpg.de

Layout

Bettina Diallo and Norbert P. Noreiks
Communication

Copyright

A split-explicit time-stepping scheme for ICON-Ocean

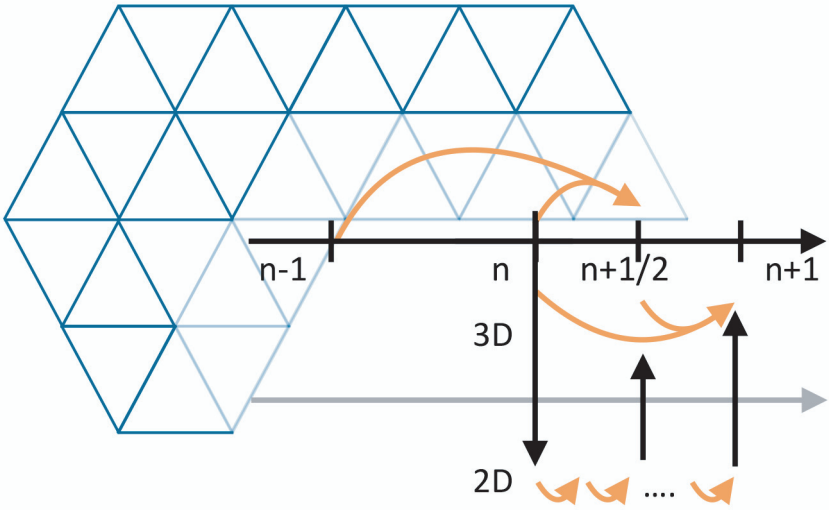

Lukas Krönert

Hamburg 2021

Lukas Krönert
aus Würzburg, Deutschland

Max-Planck-Institut für Meteorologie
The International Max Planck Research School on Earth System Modelling
(IMPRS-ESM)
Bundesstrasse 53
20146 Hamburg

Universität Hamburg
Geowissenschaften
Meteorologisches Institut
Bundesstr. 55
20146 Hamburg

Tag der Disputation: 19. Januar 2021

Folgende Gutachter empfehlen die Annahme der Dissertation:
Prof. Dr. Jochem Marotzke
Dr. Peter Korn

Vorsitzender des Promotionsausschusses:
Prof. Dr. Dirk Gajewski

Dekan der MIN-Fakultät:
Prof. Dr. Heinrich Graener

The figure on the front page presents a simulation snapshot showing the liquid water field normalized by its in-cloud value. White colors indicates cloudy air and blue colors free-tropospheric air.

Typeset using the classicthesis template developed by André Miede, available at:
https://bitbucket.org/amiede/classicthesis/

Berichte zur Erdsystemforschung / Max-Planck-Institut für Meteorologie 242
Reports on Earth System Science / Max Planck Institute for Meteorology 2021

ISSN 1614-1199

Abstract

The development and implementation of advantageous time-stepping schemes in existing ocean models bears the potential to improve the model performance in terms of higher numerical accuracy as well lower numerical costs in terms of increased stability (larger possible time-steps). Stability and accuracy of time-stepping schemes should be considered in coupled space-time discretization. In that respect, the derivation and analysis of a new space-time discretization especially within the novel spatial framework of ICON-O (ocean component of the ICON earth system model) is of significant interest.

In this thesis, adapting and implementing a split-explicit time-stepping scheme into ICON-O, we address both accuracy and stability: (a) We reduce the propagation error of barotropic signals by up to two orders of magnitude within mainly barotropic experiments. Furthermore, choosing a more advanced baroclinic time-stepping scheme results in increased accuracy of the baroclinic signal for relevant large Courant numbers. (b) The new space-time discretization shows increased numerical stability by a factor of up to 1.3 for the analysed experiments.

In addition to the new split-explicit space-time discretization based on a Leap-Frog Adams-Moulthon-3 (LF-AM3) baroclinic step, we also adapt split-explicit time-stepping for the Adams-Bashfort-2 (AB2) scheme which is originally used in ICON-O together with a semi-implicit scheme. A major effort was to bring together these time-stepping schemes with the unique spatial framework of ICON-O, which is based on a C-type staggering of variables on a triangular grid. Following this spatial framework, we preserve a mass-matrix that filters out a spurious mode and furthermore fullfill discrete conservation of volume and tracers.

In experiments with increasing complexity, we compare the two new split-explicit space-time discretizations with the original AB2 semi-implicit scheme. We show higher accuracy of the barotropic mode of the split-explicit schemes within various gravity wave experiments. In a lock-exchange experiment, we find for small Courant numbers that a coupling-error of both split-explicit time-stepping schemes results in smaller accuracy in velocity compared to the AB2 semi-implicit scheme. This coupling-error can be avoided with further improvements to the split-explicit algorithm. For desired large Courant numbers, the new LF-AM3 split-explicit space-time discretization is more accurate in the velocity, even for a time step that exceeds the stability limit of both AB2 schemes. Furthermore, the new LF-AM3 space-time discretization is more accurate for tracers independent of the Courant number. LF-AM3 shows slightly larger spurious mixing which we also find for smaller time steps with both AB2 schemes. We argue that this is caused by larger noise of the velocity on grid

scale due to smaller numerical velocity diffusion. This results in gain of control over the total velocity diffusion when using ICON-O. Within the coupled space-time discretizations of ICON-O, the new LF-AM3 split-explicit discretization shows a stability limit that is 1.3 times larger compared to the AB2 semi-implicit and up to 1.5 times larger stability limit compared to the new AB2 split-explicit discretization for our experiments.

Zusammenfassung

Die Entwicklung und Implementierung von vorteilhaften Zeitschrittverfahren für vorhandene Ozeanmodelle birgt das Potenzial, deren Ergebnis hinsichtlich höherer numerischer Genauigkeit und geringerer numerischer Kosten bezogen auf erhöhte Stabilität (größere mögliche Zeitschritte) zu verbessern. Stabilität und Genauigkeit von Zeitschrittverfahren sollten im Kontext einer gekoppelten Raum-Zeit-Diskretisierung betrachtet werden. Diesbezüglich ist die Herleitung und Analyse eines neuen Zeitschrittverfahrens innerhalb der innovativen räumlichen Diskretisierung von ICON-O (Ozeankomponente des Erdsystemmodells ICON) von bedeutendem Interesse.

In dieser Dissertation passen wir ein split-explizites Zeitschrittverfahren auf ICON-O an und implementieren dieses. Damit gehen wir die beiden Punkte Genauigkeit und Stabilität an: (a) Innerhalb überwiegend barotroper Experimente verringern wir den Fehler, der durch die Ausbreitung eines barotropen Signals entsteht, um bis zu zwei Größenordnungen. Zusätzlich wählen wir ein fortschrittliches Zeitschrittverfahren für den baroklinen Zeitschritt und verbessern damit das barokline Signal für die für uns relevanten, hohen Courant-Zahlen. (b) Die neue Raum-Zeit-Diskretisierung zeigt eine 1.3-fach erhöhte numerische Stabilität für die ausgewerteten Experimente.

Zusätzlich zu dem neuem split-expliziten Zeitschrittverfahren, welches auf einem Leap-Frog Adams-Moulthon-3 (LF-AM3) baroklinem Zeitschritt basiert, entwickeln wir das split-explizite Zeitschrittverfahren für das in ICON-O ursprünglich mit einem semi-impliziten Zeitschritt verwendete Adams-Bashfort-2 (AB2) Verfahren. Eine der großen Leistungen dieser Arbeit war das Entwickeln dieser Zeitschrittverfahren innerhalb der besonderen räumlichen Diskretisierung von ICON-O. Dieser folgend, erhalten wir die Massen-Matrix, welche eine numerische Mode aufhebt, und erfüllen diskrete Volumen- und Tracererhaltung.

In Experimenten mit ansteigender Komplexität vergleichen wir die zwei neuen split-expliziten Raum-Zeit Diskretisierungen mit dem ursprünglichen semi-impliziten AB2 Verfahren. Wir zeigen die höhere Genauigkeit der barotropen Mode beider neuer split-expliziten Verfahren anhand mehrerer Experimente von Schwerewellen. In einem Lock-exchange Experiment zeigt sich, dass für kleine Courant-Zahlen beide split-expliziten Verfahren aufgrund eines Kopplungsfehlers geringere Genauigkeit in der Geschwindigkeit haben als das semi-implizite AB2 Verfahren. Dieser Kopplungsfehler kann durch weiterführende Verbesserungen des split-expliziten Verfahrens vermieden werden. Für die üblichen großen Courant-Zahlen ist die split-explizite LF-AM3 Raum-Zeit-Diskretisierung in der Geschwindigkeit genauer, sogar außerhalb des Stabilitätslimits beider AB2 Verfahren. Zusätzlich ist LF-AM3 für Tracer, unabhängig

der Courant-Zahl, genauer. LF-AM3 zeigt ein etwas höheres numerisches Vermischen von Tracern, auch beobachtbar bei der Verwendung kleinerer Zeitschritte in den AB2 Verfahren. Wir begründen dies mit erhöhtem Rauschen in der Geschwindigkeit auf Gitterskala, bedingt durch eine geringere numerische Geschwindigkeitsdiffusion. Daraus ergibt sich für den Nutzer von ICON-O wiederum eine erhöhte Kontrolle über die gesamte Diffusion der Geschwindigkeit. Innerhalb der Raum-Zeit-Diskretisierung von ICON-O zeigt die neue split-explizite LF-AM3 Diskretisierung ein 1.3-fach höheres Stabilitätslimit als das semi-implizite AB2 Verfahren und bis zu 1.5-fache erhöhte Stabilität als die neue split-explizite AB2 Diskretisierung in den durchgeführten Experimenten.

Contents

Chapter 1

Introduction

1.1 Ocean circulation modelling

Ocean circulation models are of significant importance for oceanic and climate research. They help us understanding processes like the energy transport within the ocean or are needed for climate projection simulations (see e.g. Pörtner et al. (2019)). In current research, ocean circulation models are well established, using a large variety of numerical approaches. As such, there is ongoing research to improve these models in many aspects, including for example the choice of a horizontal mesh including grid staggering (Korn and Danilov, 2017), the advection scheme (Bernard et al., 2006), the choice of the vertical coordinate (Chassignet et al., 2006; Adcroft and Campin, 2004) and the parameterization of subgridscale processes (Griffies et al., 2010a). In particular, accuracy of the model and numerical costs are two main connected aspects in the development of the numerical schemes.

In ocean climate modelling mesocale eddies are of order 10km-100km and are often not well resolved by the numerical grid. However, since they are the most energetic eddies it is of particular interest to improve their representation in numerical models (Griffies et al., 2010a). Higher accuracy can reduce the numerical diffusion and therefore the damping of these mesoscale eddies. This higher accuracy can be achieved for example by using a higher resolution of the ocean grid or using a higher-order advection scheme. This however results generally in higher numerical costs. These costs become even more crucial in simulations with high resolution like mesoscale simulations which are performed on parallel high-performance computing systems (Koldunov et al., 2019).

The ocean circulation model used in this study is ICON-Ocean (ICON-O) Korn (2017), the ocean part of the new earth system model ICON-ESM (see e.g. Giorgetta et al. (2018), Crueger et al. (2018)) of the Max Planck Institute for Meteorology. There, the time-stepping is a semi-implicit Adams-Bashfort 2 (AB2) scheme. In this thesis, we adapt the split-explicit time-stepping scheme from Shchepetkin and McWilliams (2005) for the mathematical framework of ICON-O (Korn, 2017), which is also applied to the ocean parameterizations in Korn (2018). Based on both the time-stepping scheme from Shchepetkin and McWilliams (2005) and the spatial discretization from (Korn, 2017), we develop a new space-time discretization with the aim to increase desired larger numerical accuracy and higher stability.

1.2 Time discretization in ocean models

In general, time-dependent differential equations can be solved explicitly or implicitly (Durran, 2013). To illustrate this difference, we consider the time derivative of an arbitrary function $\partial_t f(t) = G(t)$ in simple discrete forms.

Explicit time-stepping For an explicit time-step, the right hand side $G(t)$ of a time-step t_n is only dependent of the previous time-step t_{n-1} or older time-steps. For such explicit time-step, the discrete time-derivative of a time-step size Δt can be written as

$$\frac{f_{t+\Delta t} - f_t}{\Delta t} = G(f(t), f(t-\Delta t), ..., t, t-\Delta t, ...). \tag{1.2.1}$$

The function at the new time step $f_{t+\Delta t}$ can be calculated as

$$f_{t+\Delta t} = f_t + \Delta t \; G(f(t), f(t-\Delta t), ..., t, t-\Delta t, ...). \tag{1.2.2}$$

The scheme in equation (1.2.2) describes the Euler scheme if the right hand side is only dependent on the previous time step $\mathcal{G} = \mathcal{G}(f(t), t)$.

For an explicit scheme, the Courant-Friedrichs-Lewy (CFL) stability criterion describes a stability limit α_{max}. The CFL criterion gives an upper time-step limit Δt_{max} which the time-step Δt may not exceed for a fixed grid space Δx and a velocity c. Hence in 1D, the CFL criterion can be written as

$$\frac{c\Delta t}{\Delta x} \leq \alpha_{max}. \tag{1.2.3}$$

For a larger time step than Δt_{max}, the model becomes unstable.

Implicit time-stepping In contrast to an explicit time-stepping scheme, for the implicit time-stepping the right hand side is dependent on the new time step

$$\frac{f_{t+\Delta t} - f_t}{\Delta t} = \mathcal{G}(f(t+\Delta t), t+\Delta t). \tag{1.2.4}$$

An implicit scheme is unconditionally stable, which means that it does not have a stability limit like the CFL criterion. However, solving equation (1.2.4) is more challenging and computationally more expensive than solving the explicit time-step of equation (1.2.3) with the same time step size (Durran, 2013).

Time scales in the ocean Ocean dynamics are governed by modes on many different time scales. The fastest acoustic modes are filtered out in hydrostatic models such as considered for this thesis. One can broadly distinguish between two main modes that remain in hydrostatic ocean models: On the one hand are barotropic gravity waves ($\approx 200\,\mathrm{m/s}$). They are about two orders of magnitude faster than, on the other hand, the fastest baroclinic modes, i.e. internal gravity waves ($\approx 1\mathrm{m/s}$) (Higdon and de Szoeke, 1997; Griffies et al., 2000).

In a flat-bottom ocean, a decomposition of the flow field into vertical eigenmodes, including the barotropic mode as well as baroclinic modes, is straightforward (Gill, 1982). This decomposition is less trivial in a realistic ocean with full topography. Nevertheless, also here, one can define the barotropic mode as the depth-averaged flow and the baroclinic mode as the deviation hereof (Griffies et al., 2000).

One goal of time discretizations in global ocean models is to have an explicit time step constrained by the baroclinic modes and not by the fast barotropic waves. Hence, the baroclinic modes determine the maximum time step which we name in the following baroclinic time step. Implicit time-stepping schemes are not used for the baroclinic time-step due to high numerical costs. Constraining the time step to the barotropic mode would lead to very small time steps and too high computational costs. The depth-averaged barotropic flow is of lower dimension (2D) compared to the baroclinic flow (3D) which can be exploited by solving the barotropic mode separately from the baroclinic dynamics (Higdon and de Szoeke, 1997).

Early models used a rigid lid streamfunction method (Bryan, 1969), in which the ocean surface is fixed and the barotropic dynamics are prevented. With further development of ocean models, the free-surface is considered (see e.g. Maier-Reimer et al. (1982)) and two different methods to primitive ocean equations have been established (Griffies et al., 2000).

Semi-implicit time-stepping One way is to calculate the barotropic dynamics implicitly while calculating the baroclinic dynamics explicitly. Such a semi-implicit approach is used in ICON-O Korn (2017) or in Marshall et al. (1997). This approach has several drawbacks, such as large numerical dissipation for the barotropic dynamics due to the large implicit barotropic time step.

While the representation of barotropic dynamics for the general circulation (and hence the large-scale climate) was considered not overly important for example by McWilliams (1996), this view has changed nowadays. In particular, since we know that mixing induced by barotropic tides is crucial for the global ocean circulation (Wunsch and Ferrari, 2004) and that also the geographical distribution of this mixing matters (e.g. Vic et al. (2018), MacKinnon et al. (2017)), an accurate representation of the barotropic mode receives more and more attention.

Furthermore, such an semi-implicit approach requires a linear elliptic equation to be solved which needs global communication for solving on multiple cores. This differs from the explicit scheme, where only the information of the next neighbor is needed. This global communication is supposed to be a bottleneck if simulations are performed on large numbers of cores which are needed for high resolution simulations.

Split-explicit time-stepping A different approach is a split-explicit time-stepping as in early work of Killworth et al. (1991), Bleck and Smith (1990) or Higdon and de Szoeke (1997). There, the baroclinic dynamics are stepped forward with one large baroclinic time-steps Δt. The barotropic dynamics are also solved explicitly, but with M small time-steps $\Delta t^* = \Delta t/M$. The barotropic velocity is first obtained by vertically averaging over the 3D momentum equation. Similarly, a barotropic-baroclinic coupling terms is obtained by vertically averaging over the slow-changing terms of the momentum equation. This term acts as a forcing term within barotropic

dynamics. After the 2D subcycling of the barotropic dynamics, the barotropic velocity is coupled back to the 3D velocity.

One advanced split-explicit time-stepping scheme has been developed for the Regional Ocean Modeling System (ROMS) in a profound analysis of various time stepping schemes with focus on accuracy and stability (Shchepetkin and McWilliams, 2005, 2009). This time-stepping scheme uses a Leap-Frog Adams-Moulthon-3 (LF-AM3) scheme for the baroclinic step and the Adams-Bashfort-3 Adams-Moulthon-4 (AB3-AM4) scheme for the barotropic system. Within ROMS, the LF-AM3 scheme is also used with a non-hydrostatic version of ROMS (Kanarska et al., 2007). Lemarié (n.d.) (note at CROCO website) gives a detailed description of the time-stepping algorithm for CROCO, which is based on ROMS. The LF-AM3 scheme is nowadays also used in NEMO Madec (2016) and for coastal flows in Kärnä Tuomas et al. (2013). Besides Kärnä Tuomas et al. (2013), where discontinuous Galerkin finite elements are used for an unstructured mesh, all previously mentioned models use structured grids.

Computational efficiency, stability and accuracy A larger possible Courant number/time-step size usually decreases the computational costs since fewer time steps have to be calculated for the same simulation time. The CFL criterion for the explicit time-steps varies with the dynamics and depend on the space-time discretization (Lemarié et al., 2015).

In Shchepetkin and McWilliams (2005) and Shchepetkin and McWilliams (2009), where the time-stepping scheme for ROMS is developed, the stability and accuracy are calculated based on a von Neumann linear stability analysis (Durran, 2013). While LF-AM3 shows high stability, the AB2 scheme is asymptotically unstable. However, only the time-discretization itself was analysed. An analysis of time-stepping schemes which considers a coupled space-time discretization is given in Lemarié et al. (2015). The analytical CFL number varies, depending on the advection scheme. For the second-order centered advection scheme, the stability of the LF-AM3 scheme is roughly 3 times larger than for the AB2 scheme. However, for a third-order upwind scheme, the stability of LF-AM3 is only 1.5 times larger than for AB2.

Soufflet et al. (2016) compare ROMS with NEMO Madec (2016) in a suit of baroclinic jet test cases. In this study, NEMO uses a Leapfrog temporal scheme with a modified Robert-Asselin filter (Leclair and Madec, 2009). There, ROMS, using the split-explicit time-stepping scheme as in Shchepetkin and McWilliams (2005), shows higher computational efficiency, including larger stability. Furthermore, it shows better results, presumably due to higher-order temporal and spatial discretization, for the effective resolution which defines the range upon which numerical dissipation becomes dominant.

For future high-resolution simulations which are run largely parallelized with thousands of cores, computational efficiency becomes even more important than it is today. This includes the scalability of the models as is investigated for example in Koldunov et al. (2019) for FESOM2 (Danilov et al., 2017), or Ward and Zhang (2015) for MOM from Spence et al. (2014). Solving the free-surface implicitly as done in Korn (2017) with the GMRES solver causes global communication. The CG solver shows increased scalability and is therefore more suitable Adamidis et al. (2011), but still causes this global communication. This is a bottleneck of the numerical

efficiency of high-resolutions simulations where many cores are used. Split-explicit schemes do not have global communication which is one reason why they are widely used.

1.3 Spatial discretization

Lemarié et al. (2015) perform a space-time stability analysis of the LF-AM3 and AB2 schemes within ROMS, which uses a structured grid. Instead, ICON-O uses an unstructured icosahedral grid with C-type staggering for the variables, where scalars are defined on cells centers and velocities are defined on edge midpoints. ICON-O uses a unique mathematical framework described in Korn (2017) which is also used for a shallow-water model in Korn and Linardakis (2018). In ICON-O, discrete methods from Finite Elements, Finite Volume and Mimetic Finite Differences are used. However, using C-type staggering on an unstructured grid leads to an undesired computational grid mode (Danilov, 2010; Gassmann, 2011). This grid mode appears since the degrees of freedom of scalar variables on cells is different from vector variables such as velocities which are defined on edges Danilov (2013). The grid mode has to be treated globally for an ocean model. For the icosahedral grid with C-type staggering, possibilities to control the grid mode are damping (Wan et al., 2013; Zängl et al., 2015), or filtering, (Wolfram and Fringer, 2013). However, these approaches result in an inconsistent continuity formulation. Instead ICON-O uses a mass-matrix which especially appears in the continuity equation where the grid mode is filtered out (Korn, 2017).

1.4 Software development

The development of the split-explicit time-stepping schemes within ICON-O required changes of the code throughout the dynamical core. The barotropic subcycling as well as the 2-step LF-AM3 scheme required many new routines, operators and overall changes. Even more, in ICON-O, the time-stepping scheme is embedded deeply within the code and spread over many routines. Therefore, a proper implementation within the code was one major effort of the development of the new split-explicit time-stepping schemes which included changes in the order of 10000 codes lines.

Due to the depth of code changes within ICON-O, we have not fully parallelized the new split-explicit time-stepping schemes. Therefore, we did not simulate numerically expensive experiments such as eddy resolving experiments as shown in for example Soufflet et al. (2016) and Petersen et al. (2015). Instead, we focus mainly on idealized 2D experiments in chapter 4, which are numerically less expensive.

1.5 Thesis overview

The new time-stepping scheme that we develop in this thesis is consistent within the novel space discretization of the C-type staggered icosahedral grid of ICON-O Korn (2017). The split-explicit time-stepping scheme of Shchepetkin and McWilliams (2005) is the main time-stepping scheme of our choice since it has superior stability and

accuracy towards other schemes (Lemarié et al., 2015; Soufflet et al., 2016). Therefore, we use LF-AM3 for the baroclinic step and AB3-AM4 for the barotropic step similar to Shchepetkin and McWilliams (2005). Formulating this time-stepping scheme within the spatial framework of ICON-O, we derive a new space-time discretization which is the first split-explicit scheme of a C-type staggered icosahedral grid. We ensure conservation properties while retaining the mass-matrix which filters out the grid-mode as motivated in the previous section 1.3.

Additionally to using the LF-AM3 predictor-corrector scheme for the baroclinic step, we adapt the original AB2 scheme of Korn (2017) to be used together with the AB3-AM4 barotropic subcycling. This gives us the opportunity to compare a split-explicit and semi-implicit scheme with the same AB2 baroclinic step as well as different split-explicit schemes of the baroclinic step with the same subcycling.

The baroclinic solution is updated with a fast-time averaged barotropic solution to avoid aliasing, to achieve second-order accuracy and for consistency within the discrete framework (Shchepetkin and McWilliams, 2005). We show that the solution of the fast-time averaging which is used to update intermediate velocity values introduces a coupling error that can be avoided, if the centroid of this averaging is equal to the predicted (LF-AM3) or weighted (AB2) velocity.

After diagnostic tests, we analyse accuracy and stability in idealized tests with increasing complexity. We show higher accuracy of the split-explicit schemes for various gravity wave tests. While the lock-exchange test and the overflow test are used to compare mixing between different models in Ilicak et al. (2012) and Petersen et al. (2015), we use these tests to compare different space-time discretizations of the same model. We use the lock-exchange test to analyse mixing and accuracy of the different time-stepping schemes. Further, we introduce a reduced vertical resolution which we use to analyse the stability. Lastly, we compare the results that we get to other space-time discretizations which are discussed in Lemarié et al. (2015).

This thesis is structured as follows. First, we give an overview of the ocean model equations and the spatial framework as introduced by Korn (2017), which is the basis of our new space-time discretization (chapter 2). There, we also give the discrete continuity equation of Korn (2017), which is kept for the new split-explicit time-stepping scheme.

We derive the new split-explicit space-time discretization in chapter 3. We show the continuous split-explicit form of the momentum equation and discuss the main parts of the time-stepping algorithm. We summarize all time-stepping schemes that we use.

We retain the original continuity equation and tracer equation consistently within our framework and we therefore guarantee volume and tracer conservation. Based on implications of the discrete continuity equation, we derive the new space-time discretization of the barotropic system and show a temporal averaging over the barotropic solution consistent within our spatial framework. We finalize the new space-time discretization of the discrete baroclinic step based on the LF-AM3 scheme and the discrete baroclinic step based on the AB2 scheme including a discussion of a coupling error.

In chapter 4, we analyse and discuss the new LF-AM3 and AB2 split-explicit time-stepping schemes and compare them to the old-time-stepping scheme qualitatively

and quantitatively with experiments of increasing complexity. For the analysis, we use error norms and the reference potential energy (RPE) as diagnostic tools. Simulations where we isolate the terms of the right-hand side of the momentum equation give us confidence in the new split-explicit algorithms which includes mode-splitting and the update of the baroclinic step.

We analyse the improvements of the split-explicit schemes compared to the semi-implicit scheme for highly barotropic dynamics for different gravity wave experiments. As expected, the split-explicit time-stepping schemes are more accurate since the barotropic dynamics are well resolved compared to the AB2 semi-implicit scheme.

We analyse diapycncal tracer diffusion, accuracy and stability in the lock-exchange experiment in which baroclinic dynamics are dominant compared to the barotropic dynamics. For low Courant numbers (small time step sizes), a mode-splitting error causes a decrease in accuracy for the split-explicit schemes. We introduce a configuration of the lock-exchange experiment with reduced vertical resolution so that we can analyse the stability and accuracy for relevant large Courant numbers near the stability limit. There, the LF-AM3 scheme is more accurate and shows larger stability than both AB2 schemes. Also, we see a slight increase of diapycnal diffusion for the LF-AM3 scheme. We relate this to higher accuracy and therefore a decrease of total diffusion which otherwise damps small scale noise which causes the diapycnal diffusion (Ilicak et al., 2012).

We discuss implications of the coupling error and relate the gain of stability of the LF-AM3 scheme to other space-time discretizations in Lemarié et al. (2015). We argue that due to the unstructured icosahedral grid, the gain of stability of the LF-AM3 scheme compared to the AB2 schemes differs from the gain achieved in other space-time discretizations shown in Lemarié et al. (2015).

Finally in chapter 5 we summarize the results and give a potential outlook of the split-explicit time-stepping included in ICON-O as well as potential future experiments to compare the different schemes.

Chapter 2

Ocean model equations and spatial discretization

The governing primitive ocean equations that we summarize in section 2.1 are the underlying equations that we solve. As motivated in section 1.3, a novel spatial discretization of the primitive ocean equations on a C-type staggered icosahedral grid is derived in Korn (2017). We will formulate the split-explicit time-stepping schemes based on this spatial discretization. We summarize the discrete spatial framework of ICON-O (Korn, 2017) in section 2.2. We discuss all variables and operators that we need for the discrete split-explicit discretization. Furthermore, we show the discrete continuity equation and the discrete tracer equation of ICON-O which we keep unchanged for the new split-explicit time-stepping scheme.

2.1 Governing equations

Independent of the new time-stepping scheme, we solve the primitive ocean equations in the same vector invariant form as in ICON-O (Korn, 2017) which are given in e.g. Müller (2006)

$$\frac{\partial v}{\partial t} + (f+\omega)\mathbf{z}\times v + \frac{\nabla_h |v|^2}{2} + w\frac{\partial v}{\partial z} + \frac{1}{\rho_0}\nabla_h p - \mathcal{D}_h v - \frac{\partial}{\partial z}\mathbb{A}^{\mathbf{v}}\frac{\partial}{\partial z}v = 0, \tag{2.1.1a}$$

$$\frac{\partial p}{\partial z} = -\rho g, \tag{2.1.1b}$$

$$\frac{\partial \eta}{\partial t} + \mathrm{div}_h \int_{-H}^{\eta} v dz = 0, \tag{2.1.1c}$$

$$\mathrm{div}_h v + \frac{\partial w}{\partial z} = 0, \tag{2.1.1d}$$

$$\frac{\partial c}{\partial t} + \mathrm{div}(Cv) - \mathrm{div}_h(\mathbb{K}^C \nabla_h C) - \frac{\partial}{\partial z}\mathbb{A}^C\frac{\partial}{\partial z}C = 0, \tag{2.1.1e}$$

$$\rho = F_{eos}(p, T, S). \tag{2.1.1f}$$

Here, v is the horizontal velocity, w the vertical velocity, η the free surface height, ω the vorticity, f the Coriolis parameter, C are the tracer quantities temperature T and salinity S, ρ is the water density, ρ_0 the reference density, p the hydrostatic pressure and g the gravitational constant. $\mathcal{D}_h$ is the horizontal velocity diffusion, $\mathbb{A}^{\mathbf{v}}$ the vertical velocity diffusion coefficient, $\mathbb{K}^C$ the horizontal and $\mathbb{A}^C$ the vertical diffusion for a tracer C. F_{eos} is the equation of state. $\vec{z}$ is the vertical direction vector, ∇_h the horizontal differential operator and div_h the horizontal divergence.

With the decomposition of the pressure $p = p_{hyd} + p_s$ into the sum of the internal hydrostatic pressure p_{hyd} and the surface pressure $p_s = g\rho_0\eta(x, y, t)$, equation (2.1.1a) becomes

$$\begin{aligned}\frac{\partial v}{\partial t} + (f+\omega)\mathbf{z}\times v + \frac{\nabla_h|v|^2}{2} + w\frac{\partial v}{\partial z} + \frac{1}{\rho_0}\nabla_h p_{hyd} + g\nabla_h\eta(x,y,t) \\ - \mathcal{D}_h v - \frac{\partial}{\partial z}\mathbb{A}^{\mathbf{v}}\frac{\partial}{\partial z}v = 0.\end{aligned} \tag{2.1.2}$$

The boundary of the ocean $\partial\Omega$ can be divided into the boundary at the surface $\partial\omega^s$, at the bottom $\partial\omega^b$ and at the lateral boundaries $\partial\omega^l$. The boundary conditions for the velocity are

$$\begin{aligned}&\mathbb{A}^{\mathbf{v}}\frac{\partial v}{\partial z} = \tau \text{ at } \partial\Omega^s, \quad \mathbb{A}^{\mathbf{v}}\frac{\partial v}{\partial z} = C_b|v|v \text{ at } \partial\Omega^b, \\ &v = 0 \text{ at } \partial\Omega^t, \quad w = 0 \text{ at } \partial\Omega^b, \quad w = \frac{\partial\eta}{\partial t} \text{ at } \Omega^s.\end{aligned} \tag{2.1.3}$$

Here, τ is the wind stress, tangential to the ocean. C_b is the bottom drag coefficients. The boundary conditions for the tracers are

$$\mathbb{K}^C\frac{\partial C}{\partial z} = -Q^C \text{ at}\partial\Omega^s, \quad \frac{\partial C}{\partial z} = 0 \text{ at}\partial\Omega^b, \quad \nabla_h C = 0, \text{ at}\partial\Omega^t. \tag{2.1.4}$$

Here, Q^C is the surface flux for each individual tracer C. In the idealized experiments in chapter 4 no bottom friction and surface forcing are used for the velocity and tracers. Hence, the only boundary condition that is used in the experiments is the lateral boundary condition of the velocity and tracers for the gravity wave test over an ocean mound in section 4.2.3, the lock-exchange test in section 4.3 and the overflow test in section 4.4.

2.2 Spatial framework of ICON-O

In this section, we summarize necessary parts of the discrete spatial framework of ICON-O that we use for the new discretization in chapter 3. More comprehensive details, especially regarding the mathematical framework, can be found in Korn (2017). We define all variables in section 2.2.1 and all operators in section 2.2.2 that we need for the new split-explicit time-discretization. Besides the needed operators given in Korn (2017), we define one new reconstruction operator that is needed during the barotropic subcycling.

Furthermore, we show the same discrete continuity equation in section 2.2.3 and the discrete tracer equation in section 2.2.4 as given in Korn (2017). Later, in section 3.3, we derive the new split-explicit time-stepping scheme consistent to this discrete continuity equation. Then, by keeping the discrete continuity equation and the discrete tracer equation in the same form as given in Korn (2017), we immediately guarantee volume and tracer conservation as well as constancy preservation as we discuss in sections 3.3 and 3.4.

2.2.1 Grid and variables

In ICON-O, an icosahedral grid is used with a C-type staggering of the variables. Different vertical levels are denoted with, $k \in \{1, 2, ..., k_{bot}\}$, whereas $k = 1$ denotes the surface layer and $k = k_{bot}$ the layer at the bottom of the ocean.

Each edge e of the triangle has a normal vector $\vec{n}_{e,k}$ and a tangential vector $\vec{t}_{e,k}$. For an edge between two neighbouring cells K_k and L_k, the edge midpoint is at $\vec{x}_{e_k} = \vec{x}_{K|L,k}$ with cell midpoints $\vec{x}_{K,k}$ and $\vec{x}_{L,k}$. The cell volume of a cell K is denoted as $|K|$. The length of an edge e between two cell midpoints K and L is $|e| = |K|L|$ and the length between the cell midpoints is $|e^{\perp}| = |K|L^{\perp}|$.

For the vertical grid, a z-level coordinate system is used. As such, apart from the surface layer which changes with the free-surface, all cells K at layer k have a constant thickness of $\Delta z_{K,k}$. The same holds for the thickness $\Delta z_{e.k}$ at edge e.

With the C-type staggering, the velocities are defined as their normal component on a cell edge $v_{e,k} = \vec{v}_{e,k} \cdot \vec{n}_{e,k}$. Scalars such as tracer values are defined on cell midpoints.

The cells and edges of the icosahedral grid define a so-called primal grid. Connecting the cell midpoints of the icosahedral grid results in a dual grid consisting of hexagons and pentagons (which only appear in a spherical grid and not in a regular grid such as a channel). The edges of the dual grid are called dual edges and cell centers of the dual grid are defined on the vertices of the icosahedral grid. The primal grid and the dual grid become relevant in the description of the spatial operators in the following section 2.2.2.

2.2.2 Discrete reconstruction differential operators

The discrete framework of ICON-O is based on a discrete space for normal velocities on edges and scalars on cells on the primal grid and a discrete space for scalars on cells on the dual grid. These spaces are endowed by volume weighted scalar products for scalar and vector quantities. Reconstruction operators as well as differential operators map quantities from one space to the other. For example, the result of the discrete divergence of the velocities is defined on cell centers whereas the velocities are defined on edges. Hence, the divergence maps vectors, defined at edges, to cell centers. Additionally, the discrete scalar products are used to derive transposed operators as for example the discrete gradient which is derived from the discrete divergence.

We want to emphasise, that this framework is defined in Korn (2017), where more mathematical details and explanation of this mathematical framework can be found.

In the following, we only show the operators which are used in this thesis and omit details such as the notation of the scalar product.

Discrete reconstruction operators A reconstruction operator P maps normal velocities on edges to velocity vectors on cells

$$v \to Pv_{K,k} := \frac{1}{|K|\partial z_{K,k}} \sum_{e \in \Delta K} v_{e,k}|e|(\vec{x}_e - \vec{x}_K)\Delta z_{e,k}, \tag{2.2.1}$$

while a transposed reconstruction operator maps cell velocities to edges

$$\vec{v} \to P^T \vec{v}_{K|L,k} := \begin{cases} \frac{1}{|K|L^\perp|} \left[\vec{v}_{K,k} \cdot (\vec{x}_{K|L,k} - \vec{x}_K) - \vec{v}_{L,k} \cdot (\vec{x}_{K|L,k} - \vec{x}_L)\right], & \text{if } K|L \notin \partial\mathcal{G}_k. \\ 0 & \text{else} \end{cases} \tag{2.2.2}$$

Here, $\partial\mathcal{G}_k$ describes the discrete lateral boundary of the domain Ω and describes a partial set of all edges $\mathcal{E}$ which belong to water cells

$$\begin{aligned} \partial\mathcal{G} := \{e_k = K_k|L_k \in \mathcal{E} : &\text{ exactly one of the cells } K_k \text{ or } L_k \\ &\text{which is adjacent to the edge } e_k \\ &\text{is a land cell and the other one is a water cell}\}. \end{aligned}$$

In addition to Korn (2017), we define a new reconstruction operator P^* which is similar to the reconstruction operator P, but independent of the thickness on cells and edges

$$v \to P^* v_K := \frac{1}{|K|} \sum_{e \in \partial K} v_e|e|(\vec{x}_e - \vec{x}_K). \tag{2.2.3}$$

We use this new operator for a re-formulation of the discrete continuity equation and within the discrete barotropic momentum equation.

The reconstruction operator P reconstructs a vector in a cell center out of vectors defined on the icosahedral grid. By contrast, a dual reconstruction operators $\hat{P}$ reconstructs a vector at the cell center of the dual grid $\hat{K}$, at $\vec{x}_{\hat{K}}$

$$v \to \hat{P} v_{\hat{K},k} := \frac{1}{|\hat{K}|\Delta z_{\hat{K},k}} \sum_{e \partial \hat{K}_k} v_{e,k}|e^\perp|\Delta z_{e,k}\vec{z}_{e,k} \times (\vec{x}^*_{e,k} - \vec{x}_{\hat{K},k}). \tag{2.2.4}$$

Here, $\vec{x}^*_{e,k}$ is the midpoint of the dual edge.

The transposed operator of the dual reconstruction operator reconstructs vectors at vertices to edge values

$$v \to \hat{P}^\dagger v_{\hat{K}_k|\hat{L}_k} := \begin{cases} \frac{1}{|\hat{K}_k|\hat{L}_k^\perp|} \left[\vec{v}_{\hat{K},k} \cdot (\vec{x}^*_{\hat{K}_k|\hat{L}_k} - \vec{x}_{\hat{K}_k}) - \vec{v}_{\hat{L}_k} \cdot (\vec{x}^*_{\hat{K}_k|\hat{L}_k} - \vec{x}_{\hat{L}_k})\right], & \text{if } \hat{K}|\hat{L} \notin \partial\mathcal{G}_k \\ 0 & else. \end{cases} \tag{2.2.5}$$

By applying the transposed reconstruction operator P^T of equation (2.2.2) after the reconstruction operator of P of equation (2.2.1), the mass matrix, a positive definite operator $\mathcal{M}_\mathcal{G} v_{e,k} := P^T P v_{e,k}$ is defined. $\mathcal{M}_\mathcal{G}$ maps edge quantities to the cells and back to the edges e. We also define the operators $\mathcal{M}_\mathcal{G}[f,v]_{e,k} := P^t(fPv)_{e,k}$ as a product of a scalar quantity f at cell centers with normal velocities at the edges. Similarily, we define $\hat{\mathcal{M}}_\mathcal{G}[\hat{f},v]_{e,k} := \hat{P}^\dagger(\hat{f}\hat{P}v)_{e,k}$ where $\hat{f}$ is a scalar quantity on the dual grid.

Additionally, we define the layer-thickness-independent mass matrix $\mathcal{M}^*_\mathcal{G} := P^T P^*$. M^* is new compared to the original framework and needed for the vertically integrated flux and during the barotropic subcycling. Note, that by using P^* for this mass matrix, $\mathcal{M}^*_\mathcal{G}$ is similar to the discrete formulation of Korn and Linardakis (2018), where the shallow-water equations are solved with the same discrete approach as in Korn (2017).

Discrete differential operators The discrete divergence of the velocity $\mathbf{div} v_{K,k}$ in a cell K of the vertical level k uses edge velocities $v_{e,k}$ and is a mapping from edges to cells

$$\mathbf{div}\, v_{K,k} := \frac{1}{|K|\Delta z_{K,k}} \sum_{e\in\partial K} v_{e,k}|e|n_{e,K}\Delta z_{e,k}. \tag{2.2.6}$$

Similar to the transposed reconstruction operators, the discrete gradient **grad** of a scalar quantity $f_{K|L,k}$ between the cells K and L at the vertical level k can be derived from the divergence and is a mapping from cells to edges

$$\mathbf{grad} f_{K|L,k} := \frac{f_{K,k} - f_{L,k}}{|K|L^\perp|}. \tag{2.2.7}$$

The curl is a mapping from the primal grid to the dual grid

$$\mathbf{curl}\, v_{\hat{K},k} := \frac{1}{|\hat{K}|\Delta z_{\hat{K},k}} \sum_{e\in\partial\hat{K}} v_{e,k}|\hat{e}|t_{e,k}\Delta z_{e,k}. \tag{2.2.8}$$

The vertical differential operator between two vertical levels k and $k+1$ to a half-level $k+1/2$ is

$$\mathbf{D_z} f_{K,k+1/2} := \frac{f_{K,k} - f_{K,k+1}}{\Delta z_k}. \tag{2.2.9}$$

2.2.3 Continuity equation

With the discrete differential operators from the previous section 2.2.2, the divergence free continuity equation from equation (2.1.1d) is discretized to

$$\mathbf{D}_z w_{K,k} = \frac{w_{K,k} - w_{K,k+1}}{\Delta z_{K,k}} = -\mathbf{div}\left(\mathcal{M}_\mathcal{G} v\right)_{K,k}. \tag{2.2.10}$$

Reformulating (2.2.10) and using the bottom boundary condition $w_{k_{bot}} = 0$, the vertical velocity can be obtained

$$w_{K,k} = w_{K,k+1} - \mathbf{div}\left(\mathcal{M}_\mathcal{G}[\Delta z, v]\right)_{K,k}, \quad \text{for } k = k_{bot} - 1, ..., 1. \tag{2.2.11}$$

By applying a vertical integral from the bottom layer k_{bot} to layer k we can calculate the vertical velocity as an integral over the horizontal mass fluxes

$$w_{K,k} = -\sum_{k=k_{bot}}^{k-1} \mathbf{div} \left(\mathcal{M}_{\mathcal{G}}[\Delta z, v] \right)_{K,k} . \tag{2.2.12}$$

This discretization that includes the mapping of the mass matrix $\mathcal{M}_G$ filters out the grid mode which results from the C-type staggering on the triangular grid Korn (2017). This is a key feature which we have to consider for the split-explicit time-stepping.

2.2.4 Tracer equation

Similar to the discrete continuity equation, we use the same discrete tracer equation as derived in Korn (2017). The result of the discrete tracer equation is on cells. For the ease of better readability, we omit the spatial indices in the following equation:

$$\frac{\partial (\Delta z C)}{\partial t} + \mathbf{div}\mathcal{F}(M_G [\Delta z C, v]) + \mathbf{D_z}\mathcal{F}\left[\Delta z \tilde{C} w\right] + \mathbf{div}\mathbb{K}^C \mathbf{grad} C + \mathbf{D}_Z \mathbb{A}^C \mathbf{D}_Z C = \mathcal{F}_C. \tag{2.2.13}$$

Here, $\mathcal{F}$ is the Zalesak limiter, a horizontal flux limiter (Zalesak, 1979) used for flux-corrected transport to achieve high accuracy, but to avoid over and undershoots from the tracer flux.

This discrete tracer equation is a 1-step tracer scheme. In Shchepetkin and McWilliams (2005), which our split-explicit time-stepping scheme is based on, a 2-step tracer scheme is presented. There, Shchepetkin and McWilliams (2005) calculate intermediate tracer values at time step $n+1/2$ with a focus on constancy preservation with the loss of the conservation property. Still, their tracer corrector step is both constancy preserving and conservative. Using a 2-step tracer scheme has the advantage, that the corrector step not only uses predicted velocities at $n+1/2$, but also intermediate tracer values.

For simplicity and to be able to separately analyse changes in accuracy and stability which result from a change of the momentum equation alone, we use the same discrete tracer equation as derived for ICON-O (Korn, 2017). Therefore, we keep the tracer values constant after the baroclinic LF-AM3 predictor step. Thus, we will use the tracer values of n at $n+1/2$ for the corrector step. Following Shchepetkin and McWilliams (2005), a 2-step tracer scheme is a potential future option for the new split-explicit time-stepping schemes. Then, a predictor step not only has to be added within the calculation of the tracer values, but also within the routines of the Zalesak limiter.

Chapter 3

Discrete split-explicit space-time discretization

Based on the discrete spatial framework, we derive a new discrete split-explicit space-time discretization for the primitive ocean equations in this chapter. First, we show the barotropic-baroclinic mode splitting in section 3.1, which is similarly used for all split-explicit time-stepping schemes (see e.g. Killworth et al. (1991), Bleck and Smith (1990) or Higdon and de Szoeke (1997)). Then, in section 3.2, we describe all time-stepping schemes in generalized formulations, which we will use for the baroclinic step and for the barotropic step of our new split-explicit space-time discretization.

From section 3.3 on, we develop the new space-time discretization. We discuss in section 3.3 that the continuity equation, which we keep from Korn (2017) (see section 2.2.3), defines the integrated velocity. Furthermore, we obtain a condition for a slow-changing free-surface equation. Fulfilling this condition, we argue in section 3.4 that we fulfill volume and tracer conservation. We derive the new discrete space-time discretization of the barotropic subsystem in section 3.5. We describe the fast-time averaging over the barotropic solution from Shchepetkin and McWilliams (2005) within our discretization in section 3.6. We show that we can fulfill the condition from the continuity equation for the slow-changing free-surface with this fast-time averaging within our new discretization. We finalize the new space-time discretization with the discrete baroclinic step. We derive the new discrete LF-AM3 predictor-corrector scheme (Shchepetkin and McWilliams, 2005) in section 3.7.1 and we briefly describe in section 3.7.2 the discrete baroclinic step based on the AB2 step which is used for the semi-implicit time-stepping scheme originally in ICON-O (Korn, 2017).

3.1 Barotropic-baroclinic mode splitting

As described in section 1.2, the differences in the time scales of the barotropic and the baroclinic modes can be exploited by splitting the momentum equation into a slow changing 3D baroclinic part and a fast changing 2D barotropic part as derived in previous work e.g. (Killworth et al., 1991), Bleck and Smith (1990) or Higdon and de Szoeke (1997). This mode-splitting is the basis for split-explicit time-stepping

schemes. In this section, we show the barotropic-baroclinic splitting for a vertical grid with z-coordinates. Vertical z-coordinates are used in ICON-O, where except for the top layer with changing free-surface height, all cells of a layer have constant thickness (Korn, 2017).

The total velocity v is separated into a baroclinic v' and a barotropic part $\bar{v}$

$$v = v' + \bar{v}. \tag{3.1.1}$$

The barotropic velocity is obtained by vertical integration over the velocity and division over the total depth $D = \int_{-H}^{\eta} dz$

$$v' = \frac{1}{D}\int_{-H}^{\eta} v dz = \frac{1}{D}\bar{V}. \tag{3.1.2}$$

Here, $-H$ denotes the depth of the ocean and $\bar{V}$ the vertically integrated/barotropic flux.

As such, the baroclinic velocity v' possesses no depth average

$$\int_{-H}^{\eta} v' dz = 0. \tag{3.1.3}$$

Applying the vertical integral on the momentum equation (2.1.1a) results in the equation of the barotropic flux

$$\partial_t \bar{V} + f\mathbf{z} \times \bar{V} = -gD\nabla_h \eta + \mathcal{R}, \tag{3.1.4}$$

with

$$\mathcal{R} = \int_{-H}^{\eta} dz(-\frac{1}{\rho_0}\nabla_h p_{hyd} - \mathbf{v}\cdot\nabla_h v - \omega\mathbf{z}\times v - w\frac{\partial v}{\partial z} + \mathcal{D}_h v + \frac{\partial}{\partial z}\mathbb{A}^{\mathbf{v}}\frac{\partial}{\partial z}v). \tag{3.1.5}$$

Here, $\mathcal{R}$ is called the barotropic-baroclinic coupling term. It includes all nonlinear terms and all terms which are slowly changing compared to the barotropic dynamics. During the barotropic stepping, the barotropic-baroclinic coupling term $\mathcal{R}$ is kept constant. The pressure-gradient term and the Coriolis term are the fast changing terms and are used to calculate the barotropic dynamics besides the barotropic-baroclinic coupling term. In newer models such as e.g. described in Ringler et al. (2013), the Coriolis term is included for the barotropic system whereas only the pressure gradient term is changed over the subcycling in e.g. Higdon and de Szoeke (1997).

The equation for the barotropic velocity $\bar{v}$ can be obtained by dividing the equation for the barotropic flux (3.1.4) over the total depth

$$\partial_t \bar{v} + f\mathbf{z} \times \bar{v} = -g\nabla_h \eta + \frac{1}{D}\mathcal{R}. \tag{3.1.6}$$

Substituting the barotropic mass flux $\bar{V}$ into the free surface equation (2.1.1c) gives

$$\frac{\partial \eta}{\partial t} + div_h \bar{V} = 0. \tag{3.1.7}$$

Combined, the equation for the barotropic flux (3.1.4) and the free-surface equation (3.1.7) result in the fast 2D barotropic system.

Subtracting the barotropic momentum equation (3.1.6) from the momentum equation (2.1.1a) gives the momentum equation for the baroclinic velocity

$$\begin{aligned}\frac{\partial v'}{\partial t} =& \frac{\partial v}{\partial t} - \frac{\partial \bar{v}}{\partial t} \\ =& -\omega \mathbf{z} \times v - f\mathbf{z} \times v' - \frac{\nabla_h |v|^2}{2} - w\frac{\partial v}{\partial z} - \frac{1}{\rho_0}\nabla_h p_{hyd} \\ & - g\nabla_h \eta(x,y,t) + \mathcal{D}_h v + \frac{\partial}{\partial z}\mathbb{A}^{\mathbf{v}}\frac{\partial}{\partial z}v + \frac{1}{D}\mathcal{R} \qquad (3.1.8) \\ =& \mathcal{T} - f\mathbf{z} \times \bar{v} + \frac{1}{D}\mathcal{R} \qquad (3.1.9)\end{aligned}$$

Here, $\mathcal{T}$ is the complete right-hand side of the momentum equation (2.1.1a).

The vertical z-coordinate system allows us to split the pressure gradient term between the internal dynamics and the external gravity wave highly accurately (Higdon and de Szoeke, 1997). This allows us to easily differentiate between the fast changing gradient of the free-surface and the slow changing hydrostatic pressure gradient. In models with isopycnal or terrain-following coordinates this splitting has to be treated carefully as to not lead to a large error which is called mode-splitting error (see e.g. Shchepetkin and McWilliams (2005) or Higdon and de Szoeke (1997)).

3.2 Time-stepping schemes

In this work, we will use three different time-stepping schemes. For the baroclinic time step we compare the Adams-Bashfort-2 (AB2) scheme to the Leap-Frog Adams-Moulthon-3 (LF-AM3) scheme. For the barotropic stepping we will use the Adams-Bashfort-3 Adams-Moulthon-4 (AB3-AM4) scheme. We will use these schemes similarly for the velocity and the free-surface height for the new space-time discretization of the barotropic system later in section 3.5 and for the discretization of the baroclinic momentum equation in section 3.7. Therefore, we denote the time dependent functions which can be solved by the generalized formulations of the time-stepping schemes with v and η.

Adams-Bashfort-2 The AB2 scheme which is originally used for the semi-implicit time-stepping in Korn (2017) is based on Marshall et al. (1997). AB2 is an example for a multistep method where the right-hand-side at time-step n is dependent on the older time-step (here, time step $n-1$). Similar to section 1.2, we consider the time derivative of function $\frac{\partial v(t)}{\partial t} = \mathcal{G}(v,t)$. The AB2 step is

$$v^{n+1} = v^n + \Delta t \left[\left(\frac{3}{2} + \epsilon \right) \mathcal{G}^n - \left(\frac{1}{2} + \epsilon \right) \mathcal{G}^{n-1} \right]. \qquad (3.2.1)$$

The right hand side is extrapolated in between time step n and time step $n+1$, where a nonzero ϵ leads to an offset away from the midpoint $n+1/2$. In ICON-O (Korn, 2017), as well as in this thesis we choose $\epsilon = 0.1$, since AB2 becomes unstable for $\epsilon = 0$ under inviscid conditions (Marshall et al., 1997).

Leap-Frog Adams-Moulthon-3 (LF-AM3) Shchepetkin and McWilliams (2005) investigate a variety of time-stepping schemes regarding accuracy and stability for a linear hyperbolic system

$$\frac{\partial v}{\partial t} = \mathcal{G}(v, \eta, t), \quad \frac{\partial \eta}{\partial t} = \mathcal{F}(v, \eta, t) \tag{3.2.2}$$

where $\mathcal{G} = -c\frac{\partial \eta}{\partial x}$, $\mathcal{F} = -c\frac{\partial v}{\partial x}$ and c is the phase speed. This system can be considered as a simplified form of the coupled system of the momentum equation and the free-surface equation of the primitive ocean equations which are shown in section 2.1. For this system, Shchepetkin and McWilliams (2005) derive a generalized predictor-corrector time-stepping scheme which can be simplified to a Leap-Frog Adams-Moulthon-3 (LF-AM3) scheme. LF-AM3 originally has a Leap-Frog predictor step and an Adams-Moulthon-3 corrector step. LF-AM3 can be reformulated (Shchepetkin and McWilliams, 2005) to the predictor step

$$\eta^{n+\frac{1}{2}} = \left(\frac{1}{2} - 2\gamma\right)\eta^{n-1} + \left(\frac{1}{2} + 2\gamma\right)\eta^{n} + \Delta t\ (1 - 2\gamma)\,\mathcal{F}^{n}, \tag{3.2.3}$$

$$v^{n+\frac{1}{2}} = \left(\frac{1}{2} - 2\gamma\right)v^{n-1} + \left(\frac{1}{2} + 2\gamma\right)v^{n} + \Delta t\ (1 - 2\gamma)\,\mathcal{G}^{n}, \tag{3.2.4}$$

followed by the corrector step

$$\eta^{n+1} = \eta^{n} + \Delta t\,\mathcal{F}^{n+\frac{1}{2}}, \tag{3.2.5}$$

$$v^{n+1} = u^{n} + \Delta t\,\mathcal{G}^{n+\frac{1}{2}}. \tag{3.2.6}$$

Choosing $\gamma = 1/12$ results in third order accuracy and a large stability limit (c.f. section 1.2) of $\alpha_{max} = 1.587$ (Shchepetkin and McWilliams, 2005) and is also used in e.g. Kärnä Tuomas et al. (2013). As a comparison, the AB2 scheme is asymptotically unstable if it is analysed by following the linear stability analysis of Shchepetkin and McWilliams (2005) similar to the analysis of LF-AM3. However, this analysis does not consider the coupled space-time discretization where AB2 shows also finite stability (Lemarié et al., 2015). This is expected since the AB2 scheme is successfully used in ocean circulation models (Korn and Danilov, 2017; Marshall et al., 1997). Still, also in the coupled space-time discretization, LF-AM3 shows larger stability compared to AB2 (Lemarié et al., 2015).

Due to high stability and accuracy of the LF-AM3 scheme in Soufflet et al. (2016) and Lemarié et al. (2015), we choose the LF-AM3 as the new alternative to the AB2 scheme for the baroclinic step by following the algorithmic approach of Shchepetkin and McWilliams (2005).

We note that in this formulation the Leap-Frog step as well as the Adams-Moulthon-3 step are mixed together. The symmetry of the predictor step in equation (3.2.3) and the corrector step in equation (3.2.5) of the LF-AM3 scheme is due to the reformulation of the original LF-AM3 scheme. With this reformulation, especially intermediate velocity values at time step $n + 1/2$ are obtained and are used for the discrete LF-AM3 step later in section 3.7.1.

Adams-Bashfort-3 Adams-Moulthon-4 (AB3-AM4) Similar to the generalized predictor-corrector step which can be simplified to the LF-AM3 scheme, Shchepetkin and McWilliams (2005) develop a generalized forward-backward scheme with an Adams-Bashfort-3 like forward step and an Adams-Moulthon-4 like backwards step. This AB3-AM4 scheme can be reformulated to (Shchepetkin and McWilliams, 2009)

$$\eta^{n+1} = \eta^n + \Delta t \left[\left(\frac{3}{2} + \beta \right) \mathcal{F}^n - \left(\frac{1}{2} + 2\beta \right) \mathcal{F}^{n-1} + \beta \mathcal{F}^{n-2} \right], \tag{3.2.7}$$

$$u^{n+1} = u^n - \Delta t \left[\left(\frac{1}{2} + \gamma + 2\epsilon \right) \mathcal{G}^{n+1} + \left(\frac{1}{2} - 2\gamma - 3\epsilon \right) \mathcal{G}^n + \gamma \mathcal{G}^{n-1} + \epsilon \mathcal{G}^{n-2} \right]. \tag{3.2.8}$$

Choosing the parameters $\beta = 0.281105$, $\gamma = 0.088$, $\epsilon = 0.013$ is a compromise choice within the linear stability analysis of Shchepetkin and McWilliams (2009) between large stability and second-order accuracy. The stability limit is $\alpha_{max} = 1.7802$ (Shchepetkin and McWilliams, 2009). AB3-AM4 is a suitable choice to solve the barotropic system. Besides the stability and the second-order accuracy, it has large dissipation for high velocities which filters out fast barotropic dynamics within the nonlinear system that might lead to instabilities (Shchepetkin and McWilliams, 2009). Additionally, compared to for example the LF-AM3 predictor-corrector scheme, AB3-AM4 uses only one calculation step of the right-hand side which reduces numerical costs.

3.3 Implications from continuity equation and tracer equation

From this section on, we derive the new split-explicit space-time discretization. For this new discretization, we have to ensure that the tracer fluxes are consistent with the continuity equation which connects volume fluxes and tracer fluxes. This means that using a uniform tracer field in the tracer transport equation (3.3.1) results in the discrete continuity equation (2.2.10) (Korn, 2017). To show this consistency, we closely follow the argumentation of Korn (2017). There, in the last step, the discrete free-surface equation, which is solved by the implicit solver, ensures this consistency.

Similarly, for this split-explicit discretization, we derive a slow-changing free-surface equation. However, we do not solve this equation since we solve the free-surface during the barotropic subcycling. Instead, this slow-changing free-surface equations gives us a constraint that the result of the barotropic subcycling has to fulfill to ensure the consistency between the continuity equation and the tracer equation. Additionally, this slow-changing free-surface equation defines the vertical integral that we use to calculate the barotropic flux.

For the ease of better readability, we omit some indices of the right-hand side of the following equations. Following Korn (2017), we consider a uniform tracer field $C_k^n = C$ at time step n for all cells K. With this, the discrete tracer equation (2.2.13)

without dissipative terms and without the horizontal flux limiter is

$$\frac{\Delta z_{K,k}^{n+1} C_{K,k}^{n+1} - \Delta z_{K,k}^{n} C_{K,k}}{\Delta t} = -\left\{ \mathbf{div}\left(M_G \left[\Delta z^n C, v^{n+1/2} \right] \right)_{K,k} + \mathbf{D_z}\left[\Delta z^n C w^{n+1/2} \right]_{K,k} \right\}. \tag{3.3.1}$$

Except for the surface layer with $k = 1$, the right-hand side becomes zero due to the continuity equation (2.2.10) since for the z-level coordinate system, the interior cell thickness is constant over time. For the top layer, we apply the kinematic boundary condition $w_{K,1} = \frac{\partial \eta}{\partial t}$ which leads to

$$\frac{\Delta z_{K,1}^{n+1} C_{K,1}^{n+1} - \Delta z_{K,1}^{n} C}{\Delta t} = -\left\{ \mathbf{div}\left(M_G \left[\Delta z_1^n C, v_1^{n+1/2} \right]_{K,1} \right) + \mathbf{D_z}\left[\Delta z_1^n C w_2^{n+1/2} \right]_{K,1} \right\}. \tag{3.3.2}$$

A constant tracer field should be preserved over time in all layers. To ensure this, we consider in the following a unitary tracer field $C = C_{K,1}^{n+1} = 1$. Together with applying the continuity equation to the right-hand side, this gives us an equation for the change of the surface layer thickness

$$\frac{\Delta z_{K,1}^{n+1} - \Delta z_{K,1}^{n}}{\Delta t} = w_{K,1}^{n+1/2}. \tag{3.3.3}$$

Replacing the vertical velocity with the vertical integration of the mass flux as in equation (2.2.12) results in an equation of the change of the free-surface height

$$\frac{\Delta \eta_K^{n+1} - \Delta \eta_K^{n}}{\Delta t} = -\sum_{k=k_{bot}}^{1} \mathbf{div}\left(\mathcal{M}_{\mathcal{G}}[\Delta z_k, v_k] \right)_{K,k}^{n+1/2}. \tag{3.3.4}$$

We use the definition of the mass matrix $\mathcal{M}_{\mathcal{G}}[f,v]_{e,k} = P^t f P v_{e,k}$ from section 2.2.2

$$\frac{\Delta \eta_K^{n+1} - \Delta \eta_K^{n}}{\Delta t} = -\sum_{k=k_{bot}}^{1} \mathbf{div}\left(P^T \Delta z_k P v_k \right)_{K,k}^{n+1/2}. \tag{3.3.5}$$

We can apply the thickness independent reconstruction operator P^* from equation (2.2.3) by noting that $\Delta z_{K,k} P v_{K,k} = P^* \left(\Delta z_{e,k} v_{e,k} \right)_{K,k}$ and equation (3.3.5) becomes

$$\frac{\Delta \eta_K^{n+1} - \Delta \eta_K^{n}}{\Delta t} = -\sum_{k=k_{bot}}^{1} \mathbf{div}\left(P^T P^* \left(\Delta z_{e,k} v_{e,k} \right) \right)_{K,k}. \tag{3.3.6}$$

Since $\mathbf{div}\left(P^T P^* \right)$ is independent of the layer thickness, we can apply the vertical summation before this expression

$$\frac{\Delta \eta_K^{n+1} - \Delta \eta_K^{n}}{\Delta t} = -\mathbf{div}\left(P^T P^* \sum_{k=k_{bot}}^{1} \Delta z_{e,k} v_k \right)_K^{n+1/2}. \tag{3.3.7}$$

This allows us to define the discrete barotropic flux for any time step $\tilde{n}$

$$\bar{V}_e^{\tilde{n}} = \sum_{k=k_{bot}}^{1} \Delta z_{e,k}^{\tilde{n}} v_{e,k}^{\tilde{n}}, \tag{3.3.8}$$

and we can rewrite equation (3.3.7) to

$$\frac{\Delta\eta_K^{n+1} - \Delta\eta_K^n}{\Delta t} = -\mathbf{div}\left(P^T P^* \bar{V}^{n+1/2}\right)_K. \tag{3.3.9}$$

We denote equation (3.3.4) as the equation for the slow-changing free-surface. This equation for the slow changing free surface is solved implicitly in Korn (2017). However, for the new split-explicit time-stepping scheme, we solve the free-surface during the barotropic subcycling. Hence, the equation for the slow-changing free-surface (3.3.4) leads to a constraint for the solution of the new free-surface η_K^{n+1} and the vertical integrated velocity at the intermediate $\bar{V}_K^{n+1/2}$ with the rewritten slow-changing free-surface equation (3.3.9). We fulfill this constraint by applying proper fast-time averaging over the barotropic solution which we discuss later in section 3.6.

Furthermore, equation (3.3.9) leads to the form of the free-surface equation for the barotropic system. This includes the depth-independent mass matrix $\mathcal{M}_{\mathcal{G}}^* := P^T P^*$ that we define newly for the split-explicit time-stepping schemes in section 2.2.2. If we fulfill the slow-changing free-surface equation (3.3.4) with the solution of the barotropic subcycling, then by following Korn (2017) we fulfill the consistency between the tracer equation and the continuity equation.

3.4 Volume and tracer conservation

The semi-implicit discretization by Korn (2017) is volume and tracer conservative. For the split-explicit space-time discretization developed in this thesis, we use the same 1-step tracer equation (2.2.13) and continuity equation (2.2.10). We will show in section 3.6 that the solution of the barotropic stepping also fulfills the same slow free-surface equation (3.3.4) as used in Korn (2017). Thereby, we treat the equations which are relevant for tracer and volume conservation in the same way as in Korn (2017). As such, we achieve volume and tracer conservation.

3.5 Time stepping the barotropic system

In this section we describe the new space-time discretization of the barotropic system. The algorithm is based on the time-stepping of the barotropic system which has been developed in Shchepetkin and McWilliams (2005). It is based on the AB3-AM4 scheme of equations (3.2.7) and (3.2.8).

During one baroclinic time step we subcycle M^* times over the barotropic system. The barotropic time step is $\Delta t^* = \frac{\Delta t}{M}$. Due to the time averaging over the barotropic system which will be discussed in section 3.6, the time of which we subcyle can be

up to $2\Delta t$ and the number of barotropic time steps M^* can exceed the number of barotropic time steps M between n and $n+1$, $M^* > M$.

First, we extrapolate the free-surface height and the barotropic flux to the intermediate time step $m + 1/2$. This follows the right-hand side of the AB3 step of equation (3.2.7) which is an extrapolation to the intermediate step

$$\begin{aligned} \eta_K^{m+\frac{1}{2}} &= \left(\frac{3}{2} + \beta\right) \eta_K^m - \left(\frac{1}{2} + 2\beta\right) \eta_K^{m-1} + \beta \eta^{m-2}, \\ \bar{V}_e^{m+\frac{1}{2}} &= \left(\frac{3}{2} + \beta\right) \bar{V}_e^m - \left(\frac{1}{2} + 2\beta\right) \bar{V}_e^{m-1} + \beta \bar{V}_e^{m-2}. \end{aligned} \tag{3.5.1}$$

With the solution from the extrapolated barotropic velocity, we finalize the AB3 step of equation (3.2.7) by calculating the new free surface height as described in the continuous formulation in equation (3.1.7)

$$\eta_K^{m+1} = \eta_K^m - \Delta t^* \, \mathbf{div}_K \, P^T P^* \, \bar{V}^{m+1/2}. \tag{3.5.2}$$

The equation for the new free-surface height is similar to the constraint of the slow-changing free-surface equation (3.3.4) that we derived out of the continuity equation in the previous section 3.3. In comparison to Shchepetkin and McWilliams (2005), equation (3.5.2) includes the new thickness independent mass-matrix $\mathcal{M}_{\mathcal{G}}^* := P^T P^*$ which is defined in section 2.2.2. In the following section 3.6, we will show that equation (3.5.2) allows us fulfilling the constraint of the slow-changing free-surface.

The free-surface height is interpolated with the right-hand side of the AM4 step of equation (3.2.8) to an intermediate value η'_K with

$$\eta'_K = \left(\frac{1}{2} + \gamma + 2\epsilon\right) \eta_K^{m+1} + \left(\frac{1}{2} - 2\gamma - 3\epsilon\right) \eta_K^m + \gamma \eta_K^{m-1} + \epsilon \eta_K^{m-2}. \tag{3.5.3}$$

The discrete calculation of the new barotropic flux $\bar{V}_e^{m+1}$ as shown in equation (3.1.4) finalizes the AM4 step

$$\bar{V}_e^{m+1} = \bar{V}_e^m + \Delta t^* \left[-g D_e^{m+1/2} \nabla_h \eta' - f \mathbf{k} \times \bar{V}_e^{m+\frac{1}{2}} + \mathcal{R}_e^{m+\frac{1}{2}} \right]. \tag{3.5.4}$$

Here, $D_e^{m+1/2} = \sum_{k=1}^{k_{bot}} \Delta z_{e,k}^{m+1/2} = H_e + \eta'_e$ is the interpolated total column thickness. Also, $D_e^{m+1/2}$ is defined on edge midpoints, as such η'_e are interpolated from cell values η'_K, which is calculated in equation (3.5.3) and is defined originally as a scalar value on cell midpoints.

The barotropic-baroclinic coupling term $\mathcal{R}$ of equation (3.1.5) is obtained by integrating the right-hand side of the 3D momentum equation during the baroclinic time step which we will describe in section 3.7.

As described in section 3.2, we use $\beta = 0.281105$, $\gamma = 0.088$, and $\epsilon = 0.013$ (Shchepetkin and McWilliams, 2009) except for the initial two time steps where the free-surface height and the barotropic flux of time steps $m-1$ and $m-2$ are not available. For the first barotropic step of each subcycle, we use an Euler step as described in equation (1.2.2) to calculate $\eta_K^{m+1/2}$ and $\bar{V}_e^{m+1/2}$. For the second barotropic step we set $\beta = 0$ in equation (3.5.1).

3.6 Averaging over the barotropic solution

For a baroclinic time-step Δt which advances the baroclinic momentum equation from n to $n+1$, we subcycle the barotropic system with a barotropic time-step $\Delta t^* = \frac{\Delta t}{M}$. However, the total velocity v is not updated with results of the specific barotropic time step like the barotropic flux $\bar{V}_M$ or the fast-changing free-surface η^M at the barotropic time step M.

Instead, the baroclinic system is updated with the solution of a fast-time averaging over each barotropic step m. With that, we avoid aliasing caused by such an immediate update of the baroclinic velocity, we gain consistency with the slow changing free-surface which is shown in section 3.3 and achieve second-order accuracy (Shchepetkin and McWilliams, 2005).

The fast-time averaging is a weighted integration over time with two different (primary and secondary) filters to obtain a barotropic solution for final values at $n+1$ and for intermediate values at $n+1/2$. This means, that the solutions are obtained by multiplying primary and secondary filter weights with the results of the barotropic flux and the free-surface height at each barotropic time step.

The discrete formulation of the barotropic system that we derived in section 3.5 differs from the discrete barotropic system used in Shchepetkin and McWilliams (2005) mainly because of the additional new height-free mass-matrix $\mathcal{M}^*_{\mathcal{G}} = P^T P^*$. After the definition of the filter weights, we will show that together with the new discretization of the barotropic system, we fulfill the constraint of the slow-changing free-surface equation which we need for volume and tracer conservation as well as constancy preservation.

We emphasise that for the following definitions of these filter weights, we closely follow Shchepetkin and McWilliams (2005). The primary weights have to fulfill normalization and centroid conditions

$$\sum_{m=1}^{M^*} a_m \equiv 1, \qquad \sum_{m=1}^{M^*} a_m \frac{m}{M} \equiv 1, \qquad \forall m = 1, ..., M^*. \tag{3.6.1}$$

Primary filter weights a_m are defined to calculate the barotropic solution which is used to update the baroclinic solution at t_{n+1}

$$< \eta >_K^{n+1} = \sum_{m=1}^{M^*} a_m \eta_K^m, \qquad < \bar{V} >_e^{n+1} = \sum_{m=1}^{M^*} \bar{V}_e^m = \sum_{m=1}^{M^*} D_e^m \bar{v}_e^m. \tag{3.6.2}$$

Here, a_m is a primary filter weight for the barotropic time-step m. $< . >$ denotes the solution of the primary filter weights at time-step $n+1$. M^* is the number of the last barotropic time-step where the primary filter weights are not zero. To achieve the centroid condition in equation (3.6.1), the number of barotropic time steps M^* which are calculated can be larger than the number of barotropic time-steps between n and $n+1$ so that $M^* \geq M$.

Secondary filter weights $b_{m'}$ of a barotropic time step m' are calculated from the primary weights

$$b_{m'} = \frac{1}{M} \sum_{m=m'}^{M*} a_m, \qquad \forall m' = 1, ..., M^*, \tag{3.6.3}$$

and are used for calculating the barotropic solution at the intermediate time step $t_{n+1/2}$

$$\ll \bar{V} \gg_e^{n+\frac{1}{2}} = \sum_{m'=1}^{M*} b_m \bar{V}_e^{m-\frac{1}{2}} = \sum_{m=1}^{M*} b_m D_e^{m-\frac{1}{2}} \bar{v}_e^{m-\frac{1}{2}}. \tag{3.6.4}$$

The resulting solutions of the secondary filter weights are denoted with $\ll . \gg$, and are time-centered at the intermediate time step $t_{n+1/2}$ to achieve second-order accuracy for the mass fluxes. However, we find that the secondary filter-weights are not exactly time-centered at $t_{n+1/2}$. We will discuss an error resulting from the update of theses secondary filter-weights in section 3.7.3.

In this thesis we use two different filters. The most simple filter is a rectangular filter where all primary weights are weighted equally such that $a_i = 1/M^*$. Most commonly, this filter is used with a size of twice the number of barotropic time-steps $M^* = 2M$ which is highly dissipative, whereas decreasing the filter size decreases the dissipation (Shchepetkin and McWilliams, 2005). For the experiments in chapter 4 we denote the size of the rectangular filter f_r by half the number of steps left and right from $n + 1$.

In addition to the rectangular filter, we will use the power-law shape filter based on Shchepetkin and McWilliams (2009) with p=2, q=4 and r=0.2846158 as parameters. The power-law shaped filter has negative weights for the first barotropic time-steps. This increases computational efficiency since the maximum barotropic time step M^* is only approximately 1/3 of the amount of possible time-steps between $n + 1$ and $n + 2$ compared to the rectangular filter with the full number of barotropic time steps between n and $n + 2$. Whereas second-order accuracy is lost by using a rectangular filter with smaller filter width, the power-law filter achieves second-order accuracy with above mentioned coefficients. Additionally, the power-law filter with these coefficients has little dissipation, still it provides enough damping to efficiently avoid aliasing (Shchepetkin and McWilliams, 2009).

As discussed in section 3.4, to fulfill volume and tracer conservation as well as constancy preservation, the result of the barotropic subcycling has to fulfill the constraint of the slow-changing free surface equation (3.5.2).

The results of the fast-time averaging are used as the solution of the new free-surface $\eta_K^{n+1} =< \eta >_K^{n+1}$ and the vertically integrated velocity of the intermediate time-step $\bar{V}_e^{n+1/2} =\ll \bar{V} \gg_e^{n+1/2}$. Thus, the reformulated slow-changing free-surface equation (3.3.9) can be reformulated with the results of the barotropic subcycling

$$< \eta >_K^{n+1} = < \eta >_K^n - \Delta t \, \mathbf{div} \left(P^T P^* \ll \bar{V} \gg_e^{n+1/2} \right)_K. \tag{3.6.5}$$

In Shchepetkin and McWilliams (2005), b_m are derived without the layer thickness independent mass matrix $\mathcal{M}_{\mathcal{G}}^* = P^T P^*$ which appears here in the constraint for the slow free-surface and in the fast-changing free-surface equation of the discrete barotropic system (3.5.2). Following the derivation of $b_{m'}$ by Shchepetkin and McWilliams (2005), we show that the expression of $b_{m'}$ in equation (3.6.3) still fulfills the constraint (3.6.5) if we include the mass matrix $\mathcal{M}_{\mathcal{G}}^*$ in the equations for the free surface.

During the barotropic subcycling, the free-surface at time step m is obtained by summing over all previous time-steps m' of equation (3.5.2).

$$\eta_K^m = \eta_K^0 - \frac{\Delta t}{M} \sum_{m'=1}^{m-1} \mathbf{div} \left(P^T P^* \, \bar{V}_e^{m'+1/2} \right)_K \tag{3.6.6}$$

We integrate the barotropic free-surface height over the full barotropic subcycling with the primary filter weights a_m (see equation (3.6.2)) for all barotropic steps M^* , starting at the baroclinic time step n (where $m = 0$). We use equation (3.6.6) for the result of the barotropic free-surface height η_m at each barotropic step m. This results in the fast-time averaged solution of the free-surface height at the new baroclinic time-step $n + 1$

$$< \eta >_K^{n+1} = \eta_K^n - \sum_{m=1}^{M^*} a_m \eta_K^m \tag{3.6.7}$$

$$= \eta_K^n - \sum_{m=1}^{M^*} a_m \frac{\Delta t}{M} \sum_{m'=1}^{m} \mathbf{div} \left(P^T P^* \, \bar{V}^{m-1/2} \right)_K \tag{3.6.8}$$

$$= \eta_K^n - \frac{\Delta t}{M} \sum_{m=1}^{M^*} a_m \sum_{m'=1}^{m} \mathbf{div} \left(P^T P^* \, \bar{V}^{m-1/2} \right)_K \tag{3.6.9}$$

$$= \eta_K^n - \frac{\Delta t}{M} \mathbf{div} \left[P^T P^* \left(\sum_{m=1}^{M^*} a_m \sum_{m'=1}^{m} \bar{V}^{m-1/2} \right) \right]_K . \tag{3.6.10}$$

Shchepetkin and McWilliams (2005) show that

$$\sum_{m=1}^{M^*} a_m \sum_{m'=1}^{m} \bar{V}^{m'-1/2} = \sum_{m''=1}^{M^*} \bar{V}^{m''-1/2} \sum_{m=m''}^{M^*} a_m, \tag{3.6.11}$$

where m'' is introduced as an additional summation index of a barotropic step.
Using this and noting that the initial free surface height η_K^n is set equal to the barotropic solution of the free-surface height of the old time step $\eta_K^n =< \eta >_K^n$, equation (3.6.7) becomes

$$< \eta >_K^{n+1} =< \eta^n >_K - \frac{\Delta t}{M} \mathbf{div} \left[P^T P^* \left(\sum_{m''=1}^{M^*} \bar{V}^{m''-1/2} \sum_{m=m''}^{M^*} a_m \right) \right]_K \tag{3.6.12}$$

$$=< \eta^n > - \Delta t \, \mathbf{div} \left[P^T P^* \left(\sum_{m''=1}^{M^*} \bar{V}^{m''-1/2} \frac{1}{M} \sum_{m=m''}^{M^*} a_m . \right) \right]_K . \tag{3.6.13}$$

With b_m from equation (3.6.3), rewriting m'' as m' and using equation (3.6.4), where the secondary filter weights are used for calculating the intermediate velocity, we get

$$< \eta >_K^{n+1} =< \eta >_K^n - \Delta t \, \mathbf{div} \, P^T P^* \sum_{m''=1}^{M^*} \bar{V}_e^{m''-1/2} b_{m''} \tag{3.6.14}$$

$$=< \eta >_K^n - \Delta t \, \mathbf{div} \, P^T P^* \ll \bar{V} \gg_e^{n+1/2} . \tag{3.6.15}$$

Hence, with a_m and b_m as defined above we fulfill the constraint of the slow changing free surface equation (3.6.5) and (3.5.2). As such, we achieve constancy preservation as well as volume and tracer conservation as discussed in sections 3.3 and 3.4.

3.7 Time stepping the baroclinic system

3.7.1 LF-AM3

As discussed in section 3.2, we use the Leap-Frog Adams-Moulthon-3 (LF-AM3) scheme as the main new split-explicit space-time discretization since LF-AM3 shows larger accuracy and larger stability compared to a baroclinic step based on an Adams-Bashfort-2 (AB2) scheme (Shchepetkin and McWilliams, 2005; Lemarié et al., 2015; Soufflet et al., 2016) which is originally used for the semi-implicit scheme of ICON-O (Korn, 2017). We have shown LF-AM3 in equations (3.2.3) to (3.2.6) which is originally derived for the linear hyperbolic system (3.2.2) (Shchepetkin and McWilliams, 2005).

In the following, we show the new space-time discretization of the LF-AM3 baroclinic step based on the time-stepping algorithm of Shchepetkin and McWilliams (2005) while following closely the spatial discretization of ICON-O (Korn, 2017). The discrete operators that we use are summarized in section 2.2.2.

First, the velocity at $n + 1/2$ is calculated with the Leap-Frog predictor step of equation (3.2.4)

$$v_{e,k}^{n+\frac{1}{2}} = \left(\frac{1}{2} - 2\gamma\right) v_{e,k}^{n-1} + \left(\frac{1}{2} + 2\gamma\right) v_{e,k}^{n} + \Delta t \, (1 - 2\gamma) \, \mathcal{G}_{e,k}^{n} \tag{3.7.1}$$

where the continuous right-hand side is

$$\mathcal{G}(v) = -(f + \omega)\mathbf{z} \times v - \frac{\nabla_h |v|^2}{2} - w\frac{\partial v}{\partial z} - \frac{1}{\rho_0}\nabla_h p_{hyd} - \mathcal{D}_h v + \frac{\partial}{\partial z}\mathbb{A}^{\mathbf{v}}\frac{\partial}{\partial z} v, \tag{3.7.2}$$

and the discretized right-hand side is

$$\begin{aligned}\mathcal{G}_{e,k}(v) = &-\hat{\mathcal{M}}_{\mathcal{G}} \left[(f + \omega)\mathbf{z}, v\right]_{e,k} - \mathcal{M}_G \, \mathbf{grad} \left[\frac{|\mathcal{P}_G v|^2_{\mathbb{R}^3}}{2}\right]_{e,k} - \mathcal{P}_G^T \mathcal{Q}_G \left(w \mathbf{D}_{\mathbf{z}} \mathcal{P}_G v\right)_{e,k} \\ &- \mathcal{M}_G \, \left(\mathbf{grad} \, p_{hyd}\right)_{e,k} + \mathcal{K}^{\mathbf{v}} \left(\mathbf{grad} \, \mathbf{div} \, v - \mathbf{curl}^T \mathbf{curl} \, v\right)_{e,k}.\end{aligned} \tag{3.7.3}$$

For the ease of better readability, we omit some indices in this and following equations. Considering the kinematic boundary condition similar to equation (3.3.3), the predicted free-surface height is

$$\eta_K^{n+1/2} = \left(\frac{1}{2} - 2\gamma\right) \eta_K^{n-1} + \left(\frac{1}{2} + 2\gamma\right) \eta_K^{n} + \Delta t \, (1 - 2\gamma) \, w_{K,1}. \tag{3.7.4}$$

As described in section 3.2, we use $\gamma = 1/12$ to achieve third order accuracy and large stability (Shchepetkin and McWilliams, 2005).

Compared to the momentum equation (2.1.1a) of the primitive ocean equations, the right-hand side of the equation of the predicted velocity (3.7.1) does not contain the gradient of the free-surface height and also not the vertical velocity diffusion. The gradient of the free-surface height is a purely barotropic term and is only calculated during the barotropic subcycling. The vertical diffusion is calculated implicitly and only calculated for the final velocity $v_{e,k}^{n+1}$ after the baroclinic stepping.

Additionally, compared to the continuous form of the baroclinic momentum equation (3.1.8), we do not subtract the barotropic-baroclinic coupling term $\mathcal{R}$ (the vertical integrated right-hand side). The barotropic-baroclinic coupling term is only needed for the barotropic subcycling at the intermediate time-step $n+1$ to achieve second-order accuracy.

Therefore, for a sufficiently large time step, the predicted velocity $v^{n+1/2}$ violates the CFL criterion. To obtain the barotropic-baroclinic coupling term at the intermediate step, we have two possibilities. One option is to extrapolate the coupling term itself to time $n+1/2$ from the right-hand side of time steps n and older. Then, the predicted velocity is corrected after the barotropic subcycling with the solution of the secondary filter weights (Lemarié, n.d.; Demange et al., 2019; Shchepetkin and McWilliams, 2005).

The other option is to extrapolate the barotropic flux (or the barotropic velocity). If a 2-step tracer scheme is used, tracer conservation and constancy preservation are easier to fulfill for this option (Shchepetkin and McWilliams, 2005). We follow this approach, as such a 2-step tracer scheme is a possible future development of the new split-explicit space-time discretization.

We extrapolate the barotropic velocity with

$$V_e^{n+1/2} = 2V_e^n - V_e^{n-1/2} = 2 \ll V \gg_e^n - \ll V \gg_e^{n-1/2} . \tag{3.7.5}$$

This result is used to correct the predicted velocity of equation (3.7.1)

$$v_{e,k}^{n+1/2} = \tilde{v}_{e,k}^{n+1/2} + \left(V_e^{n+1/2} - \int \tilde{v}_{e,k}^{n+1/2} \, \mathrm{dz} \right) / D_e^{n+1/2}, \tag{3.7.6}$$

where $D_e^{m+1/2} = \sum_{k=1}^{k_{bot}} \Delta z_{e,k} k^{m+1/2} = H_e + \eta_e^{n+1/2}$ is the interpolated total column thickness on edges similar to section 3.5. We note that $\tilde{v}_{e,k}^{n+1/2}$ of the right-hand side of equation (3.7.6) is the predicted velocity of equation (3.7.1), whereas $v_{e,k}^{n+1/2}$ on the left-hand side is the corrected velocity at the intermediate time step. The vertical integral of the velocity is calculated as shown in equation (3.3.8).

The barotropic-baroclinic coupling term is obtained by vertically integrating the sum of all terms after calculating the right-hand side of equation (3.7.3) at $n+1/2$. The barotropic-baroclinic coupling term becomes

$$\begin{aligned} \mathcal{R}_{e,k}^{n+1/2} = \sum_{k=1}^{k_{bot}} \Delta z_{e,k}^{n+1/2} \Bigg(& -\hat{\mathcal{M}}_{\mathcal{G}} \left[(f+\omega)\mathbf{z}, v \right]_{e,k} - \mathbf{grad} \left[\frac{|\mathcal{P}_G v|_{\mathbb{R}^3}^2}{2} \right]_{e,k} - \mathcal{P}_G^T \mathcal{Q}_G \left(w \mathbf{D_z} \mathcal{P}_G v \right)_{e,k} \\ & - \mathbf{grad} \left(p_{hyd} \right)_{e,k} + \mathcal{K}^{\mathbf{v}} \left(\mathbf{grad}\, \mathbf{div}\, v - \mathbf{curl}^T \mathbf{curl}\, v \right)_{e,k} \Bigg)^{n+1/2} . \end{aligned}$$

(3.7.7)

As discussed in section 2.2.4, Shchepetkin and McWilliams (2005) use a two-step tracer scheme where tracer values are calculated at the $t_{n+1/2}$, whereas we use the original 1-step tracer scheme of Korn (2017). As such, we keep the tracer values C for the barotropic-baroclinic coupling term and the corrector step constant at $t_{n+1/2}$ so that $C^{n+1/2} = C^n$.

Now, $\mathcal{R}_{e,k}^{n+1/2}$ is used as the constant barotropic-baroclinic coupling term to solve the barotropic system as described in section 3.5. Afterwards, the corrector step of the baroclinic system can be computed. However, the right-hand side at $t = n + 1/2$, as used for the barotropic-baroclinic coupling term in equation (3.7.7), will not be computed a second time for the corrector step. Therefore, the barotropic system can also be calculated after the corrector step, which is

$$v_{e,k}^{n+1} = v_{e,k}^{n} + \mathcal{G}_{e,k}^{n+1/2} \Delta t. \tag{3.7.8}$$

The continuous right-hand side of the corrector step is

$$\begin{aligned} \mathcal{G}_{e,k}^{n+1/2}(v) = \Bigg\{ & -(f+\omega)\mathbf{z} \times v - \frac{\nabla_h |v|^2}{2} - w\frac{\partial v}{\partial z} \\ & - \frac{1}{\rho_0}\nabla_h p_{hyd} + \mathcal{D}_h v + \frac{\partial}{\partial z}\mathbb{A}^{\mathbf{v}}\frac{\partial}{\partial z} v \Bigg\}^{n+1/2} \end{aligned} \tag{3.7.9}$$

and the discrete right-hand side becomes

$$\begin{aligned} \mathcal{G}_{e,k}^{n+1/2}(v) = \Bigg\{ & -\hat{\mathcal{M}}_{\mathcal{G}} \left[(f+\omega)\mathbf{z}, v\right]_{e,k} - \mathbf{grad}\left[\frac{|\mathcal{P}_G v|_{\mathbb{R}^3}^2}{2}\right]_{e,k} - \mathcal{P}_G^T \mathcal{Q}_G \left(w \mathbf{D_z} \mathcal{P}_G v\right)_{e,k} \\ & - \mathbf{grad}\left(p_{hyd}\right)_{e,k} + \mathcal{K}^{\mathbf{v}}\left(\mathbf{grad}\,\mathbf{div} v - \mathbf{curl}^T \mathbf{curl} v\right)_{e,k} + \mathbf{D_{\bar{z}}} \mathcal{A}^{\mathbf{v}} \mathbf{D_z} v_{e,k} \Bigg\}^{n+1/2}. \end{aligned} \tag{3.7.10}$$

Compared to the predictor step in equation (3.7.1), the vertical velocity diffusion is included within the corrector step and solved implicitly for v^{n+1}. The final new horizontal velocity is corrected with the results from the primary filter weights of the barotropic subcycling

$$v_{e,k}^{n+1} = \tilde{v}_{e,k}^{n+1} + \left(< V >_e^{n+1} - \int \tilde{v}_{e,k}^{n+1} \,\mathrm{dz} \right) / D_e^{n+1}. \tag{3.7.11}$$

Similar to the correction of the intermediate velocity in equation (3.7.6), $\tilde{v}_e^{n+1}$ of the right-hand side is the uncorrected velocity and v_e^{n+1} on the left-hand side is the corrected velocity.

To achieve higher accuracy, the intermediate velocity which transports the tracers is obtained by an additional interpolation

$$v_{e,k}^{n+1/2} = \frac{3}{4} v_{e,k}^{n+1/2} + \frac{v_{e,k}^{n} + v_{e,k}^{n+1}}{8}, \tag{3.7.12}$$

and corrected once more, now with the result from the secondary filter-weights

$$v_{e,k}^{n+1/2} = v_{e,k}^{n+1/2} + \left(\ll V \gg_e^{n+1/2} - \int v_{e,k}^{n+1/2} \, \mathrm{dz} \right) / D_e^{n+1/2}. \tag{3.7.13}$$

As Shchepetkin and McWilliams (2005) do not describe this interpolation in detail, we follow the interpolation of ROMS UCLA (Florian Lemarié, personal communication, May 04, 2020). We calculate the vertical velocity from the continuity equation (2.2.12) and lastly we transport the tracers with equation (2.2.13).

For the initial time step of a simulation, since no values at $n-1$ are available, we use an Euler step as described in equation (1.2.2) to advance to the intermediate values.

3.7.2 Adams-Bashfort-2 (AB2)

In the above section, we described the new split-explicit time-stepping algorithm with a LF-AM3 baroclinic step. However, the original semi-implicit scheme uses an AB2 step as shown in equation (3.2.1) for the momentum equation (Korn, 2017). For a comparison between a semi-implicit scheme and a split-explicit scheme which use the same baroclinic time step, we also derive the split-explicit algorithm for the AB2 scheme.

This means that the baroclinic step from n to $n+1$ is based on the AB2 scheme. For the barotropic subcycling, we use the same AB3-AM4 scheme as described in section 3.5. In the following, we briefly summarize the algorithm of the new AB2 split-explicit space-time discretization.

The right-hand side is calculated as in equation (3.7.3) and extrapolated to $n+1/2+\epsilon$.

$$\mathcal{G}_{e,k}^{n+1/2} := \left(\frac{3}{2} + \epsilon \right) \mathcal{G}_{e,k}^{n} - \left(\frac{1}{2} - \epsilon \right) \mathcal{G}_{e,k}^{n-1}, \tag{3.7.14}$$

where $\epsilon = 0.1$ as discussed in section 3.2 to avoid instabilities (Marshall et al., 1997). $\mathcal{G}^{n+1/2}$ is used to calculate the uncorrected velocity at time step $n+1$

$$v_{e,k}^{n+1} = v_{e,k}^{n} + \mathcal{G}_{e,k}^{n+1/2} \Delta t. \tag{3.7.15}$$

For the barotropic subcycling, the barotropic-baroclinic coupling term is calculated by vertically integrating $\mathcal{G}^{n+1/2}$ similar to equation (3.7.7). The barotropic system is subcycled from n to $n+1$ as described in section 3.5 in the same way as for the LF-AM3 baroclinic step. With the results from the barotropic subcycling, the velocity at $n+1$ is corrected as in equation (3.7.11). For the LF-AM3 scheme, the intermediate velocity which is used for the tracer advection is interpolated as in equation (3.7.12) by using the predicted velocity at time step $n+1/2$. This predicted velocity does not exist for the AB2 scheme. Thus, we interpolate the intermediate velocity which is needed for the tracer advection as follows

$$v_{e,k}^{\gamma} = \gamma v_{e,k}^{n+1} + (1-\gamma) v_{e,k}^{n}, \tag{3.7.16}$$

where $\gamma = 0.6$ which is similar to $\epsilon = 0.1$ for the extrapolation of the right-hand side. The intermediate velocity is corrected with the solution of the secondary filter

weights from the subcycling with equation (3.7.13). The result is used to calculate the vertical velocity from the continuity equation (2.2.12) and the new tracers can be calculated with equation (2.2.13).

With the AB2 split-explicit scheme, on the one hand, we have a comparison between a semi-implicit scheme and a split-explicit scheme where only the method to solve the barotropic modes is different. On the other hand, we can compare two different split-explicit time-stepping schemes which use the same barotropic scheme.

3.7.3 Coupling error of the barotropic update

The time-averaging filters, described in section 3.6, are needed to avoid aliasing and to achieve second-order accuracy of the mass fluxes (Shchepetkin and McWilliams, 2005). Together, the results of the primary and secondary filter weights have to fulfill the constraint for the slow-changing free-surface equation (3.6.5).

We find out, that the secondary filter weights are actually not centered at $n + 1/2$. Instead, the center of the weights is positioned beyond $n + 1/2$, depending on the applied filter. We show this in a small example, where we consider a rectangular filter with $M = 2$ barotropic steps from n to $n + 1$ and a rectangular filter width $f_r = 1$.

For this rectangular filter, the total number of the nonzero filter weights is $2\,f_r + 1$. The resulting filter weights are used for barotropic time steps at $n, n + 0.5, n + 1$, where for example the barotropic time step at $n + 1$ goes from $n + 1$ to $n + 1.5$. The total number of barotropic steps is $M^* = 3$ and the final, non time-averaged barotropic solution $\bar{V}$ of the subcycling, is beyond $n + 1$. With the rectangular filter, all weights of the primary filter are constant which are $a_i = 1/3$, $\forall i \in \{1, 2, 3\}$. These primary weights fulfill the centroid and normalization conditions of equation (3.6.1). The resulting secondary filter weights are $b_1 = 1/2$, $b_2 = 1/6$, $b_3 = 1/6$ and also fulfill the normalization condition.

However, the centroid of these secondary weights, calculated by equation (3.6.3), is positioned at $n + 10/12$. This off-centering from $n + 1/2$ of the secondary weights differs depending on the filter shape and number of barotropic steps. It decreases for larger numbers of barotropic time steps M as well as for smaller rectangular filter width. The power-law filter of Shchepetkin and McWilliams (2005) that we also use (see section 3.6) is more accurate by fulfilling the centroid condition of the secondary filter weights than the rectangular filter with a large filter width.

For the LF-AM3 scheme, the baroclinic solution of the predictor step is at $n + 1/2$. So, the barotropic solution of the secondary filter weights is shifted in time compared to this baroclinic solution. This introduces an error if we sum the barotropic and the baroclinic velocity to calculate the total velocity at the intermediate time step. This total velocity at $n + 1/2$ is used to calculate the tracer flux from n to $n + 1$ with equation (2.2.13). We note that for the AB2 scheme this is different, since the intermediate velocity is not predicted at $n + 1/2$, but interpolated at $n + 0.6$ as discussed in section 3.7.2. Still, a shift between this interpolated error and the barotropic solution causes a similar error.

In our algorithm, we do not step forward the baroclinic velocity with a right-hand-side which has no barotropic component . Instead, we use the full right-hand side

(baroclinic and barotropic) and correct the solution of the full velocity with the barotropic solution from the subcycling. We describe the coupling error by considering a case where the fast changing barotropic terms are zero and the barotropic-baroclinic coupling term is the dominant barotropic dynamic. In this case, we predict the intermediate velocity correctly at $n + 1/2$, since we include the barotropic-baroclinic coupling term in the predictor step. However, afterwards we correct this result with a barotropic solution that is shifted in time which introduces a small error.

Regarding the time-stepping schemes, we see that this error for both split-explicit schemes (AB2, LF-AM3) is negligible compared to the AB2 semi-implicit scheme if the semi-implicit scheme itself shows a larger error of the barotropic dynamics because of the implicit damping as we will show in an experiment in section 4.2.3. For this experiment, the error of the velocity and the free-surface height of both split-explicit schemes is smaller compared to the error of the AB2 semi-implicit scheme since the split-explicit schemes calculate the overall fast barotropic dynamics even with this coupling error more accurate than the semi-implicit scheme.

Compared to that, we see a larger error of the split-explicit schemes compared to the AB2 semi-implicit scheme for the lock-exchange experiment in section 4.3 for small Courant numbers/time step sizes. In this experiment, the fast changing barotropic dynamics are small compared to the barotropic-baroclinic coupling term. For small Courant numbers, the semi-implicit scheme resolves the dynamics well since no relevant barotropic dynamics could be damped by the implicit scheme. For this case, the split-explicit schemes show larger errors in the velocity due to the coupling error compared to the semi-implicit scheme.

However, we will argue that this error is only noticeable for small Courant numbers/time steps. Accordingly, we find that especially the LF-AM3 scheme is more accurate than both AB2 schemes for large Courant numbers. Additionally, small Courant numbers are not intended in ocean general circulation models because of high numerical costs.

Still, this error can be avoided by developing filters for the LF-AM3 scheme which centers the barotropic solution of the secondary filter weights at $n + 1/2$. Similarly, for the AB2 scheme, filters should be used which center the barotropic solution of the secondary filter weights at $n + 0.6$.

Chapter 4

Experiments and analysis

In this chapter, we analyse and discuss the new AB2 and LF-AM3 split-explicit space-time discretizations and compare them to the old AB2 semi-implicit scheme.

We start with introducing metrics in section 4.1 that we use to asses the accuracy of the new discretizations. These are the maximum norm and the root mean square norm. Additionally, we calculate the reference potential energy (RPE) to analyse spurious tracer mixing. Afterwards, we present performance tests, where we isolate slow-changing terms of the right-hand side. These tests give us confidence in the new split-explicit algorithms including the mode-splitting and the update of the baroclinic step.

After these diagnostic tests, we analyse accuracy and stability in idealized tests with increasing complexity. As discussed in section 1.4, the split-explicit time-stepping schemes have not been fully parallelized yet. Therefore, we choose mainly 2D (and one 3D) experiments which can be solved on a single core within reasonable time.

We analyse the improvements of the split-explicit schemes compared to the semi-implicit scheme for highly barotropic dynamics for different gravity wave experiments in section 4.2. We start with a simple gravity wave which can be considered as a 1D experiment. Next, we simulate a gravity wave on an aqua planet, which allows us to compare the discretizations in a 3D geometry, where the Coriolis force is included. This is excluded in all other experiments which are considered as 2D experiments. Afterwards, we calculate a gravity wave in 2D where we add a steep ocean mound as bathymetry. Whereas the gravity wave experiments are highly driven by the barotropic mode, including the ocean mound adds an additional barotropic-baroclinic coupling. In this experiment, due to the additional baroclinic dynamics, the time-step is restricted and we analyse the stability of the different discretizations besides the accuracy as in the previous experiments.

In section 4.3 we analyse differences in the results of the tracers and velocity for the lock-exchange experiment. There, the barotropic dynamics are small compared to the baroclinic dynamics. We compare diapycnal tracer mixing of the different space-time discretizations with the reference potential energy. We discuss the accuracy in velocity and temperature as well as the bias caused by the coupling error. We discuss qualitatively the overflow experiment in section 4.4 where an additional topography is included.

We follow with a discussion of the experiments in section 4.5. We discuss the implication of the coupling error and relate the gain of stability of the LF-AM3 scheme to other space-time discretizations in Lemarié et al. (2015).

4.1 Diagnostics

4.1.1 Error norms

We use the maximum norm and the root mean square norm (see e.g. Peixoto and Barros (2014)) to calculate global errors. With n_K being the number of triangular cells, the maximum norm of a cell variable f_K is

$$E_{\max}(f_{K,\mathrm{hr}}, f_K) = \max_{K=1,\dots,n_K} ||f_{K,\mathrm{hr}} - f_K||, \tag{4.1.1}$$

and the root mean square norm is

$$E_2(f_{K,\mathrm{hr}}, f_K) = \sqrt{\left(\frac{\sum_{K=1}^{n_K} ||f_{K,\mathrm{hr}} - f_K||^2}{n_K}\right)}. \tag{4.1.2}$$

Here, $f_{K,hr}$ is the solution of a simulation with a very small time-step (high resolution in time) functioning as a reference value as the simulations converge to this solution with decreasing time step.

4.1.2 Reference potential energy (RPE)

To analyse spurious mixing, we use the reference potential energy (RPE) which is originally discussed in Winters et al. (1995) and calculate it for the lock-exchange experiment later in section 4.3. This experiment is part of a suit of test cases, defined and analysed in Ilicak et al. (2012), to examine spurious dianeutral transport. Also, they are used for the analysis of an arbitrary Lagrangian-Eulerian vertical coordinate in Petersen et al. (2015). Note that in Petersen et al. (2015) RPE is also called resting potential energy.

First, the density $\rho(x, y, z)$ is sorted in a 1D array such that the sorted density $\rho^*(z)$ decreases from bottom to top. The resulting RPE is calculated by a volume integration over that column:

$$\mathrm{RPE} = g \int z\rho^*(z) dV \tag{4.1.3}$$

The RPE can be interpreted as a measure of mixing due to spurious numerical or physical processes. Over time, with increased mixing of the density, the RPE increases. To measure mixing, the RPE method can only be applied for nonzero buoyancy fluxes (Griffies et al., 2000) and without surface forcing (Ilicak et al., 2012). The lock-exchange experiment is within these limits.

The normalized change of the RPE from its initial value is analysed and plotted

$$\frac{\mathrm{RPE}(t) - \mathrm{RPE}(t=0)}{\mathrm{RPE}(t=0)} \tag{4.1.4}$$

For the implementation of the RPE, we follow the scripts of Petersen (2019), which are used for Petersen et al. (2015).

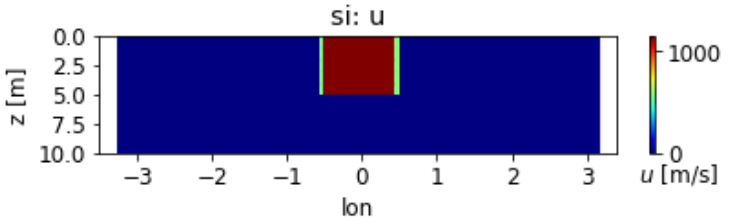

Figure 4.1: Initial state of the lateral velocity for the tests with isolated terms of the right-hand side.

4.1.3 Isolated terms

To get confidence in the new algorithm, we calculate the evolution of several slow-changing terms of the right-hand side of the momentum equation for the baroclinic step. These terms are the rotational part of the horizontal velocity advection $\omega \mathbf{z} v$, the gradient of the kinetic energy $\frac{\nabla_h |v|^2}{2}$ and the horizontal velocity diffusion $\mathcal{D}_h v$. The horizontal viscosity coefficient is $10^{10} m^s/s$. All of these terms contribute to the constant barotropic-baroclinic coupling term.

We use a toroidal grid with a length of $3.16 \cdot 10^7$ km in the longitudinal direction. This test is a 2D (x/z coordinates) experiment. We use periodic boundaries in the third y-dimension in which the variables (vectors and scalars, such as velocity, free-surface height and tracers) are constant as we use zero Coriolis force. This configuration allows us to analyse the different schemes in idealized 2D experiments with the full 3D code.

The experiments use 10 layers, each with a layer thickness of 1m. Within the upper fiver layers, between $+/-30°$ longitude, a constant velocity of $1 \cdot 10^3$ m/s is initialized. The initial velocity can be seen in figure 4.1. The velocity is remapped backwards from the edges to the cell centers. Therefore, a small smoothed boundary can be seen where the velocity is initialized. By initializing the velocity only within half of the vertical levels, we can test the barotropic-baroclinic coupling. An incorrect coupling would result in a nonzero velocity immediately in all lower layers. Except for the vertical advection term, we see only changes within the upper five layers since all these dynamics act only in the lateral direction. If not otherwise stated, we use $M = 10$ barotropic steps and a rectangular filter width of $f_r = 0$ for the new split-explicit time-stepping schemes.

In figure 4.2 we compare the E_2 root mean square norm of the velocity between the LF-AM3 split-explicit time-stepping scheme and the AB2 semi-implicit scheme. We run all schemes for the time steps $\Delta t = \{1\,\text{h}, 10\,\text{min}, 1\,\text{min}\}$. The high resolution simulation which we use to calculate the E_2 norm is an AB2 semi-implicit simulation with the time step $\Delta t = 1\,\text{s}$.

For all dynamics which are exclusively within the lateral direction, the AB2 split-explicit scheme is equal to the AB2 semi-implicit scheme. For these terms, the error of the LF-AM3 scheme is similar to the error of the AB2 schemes. For the test of the vertical advection term, the AB2 split-explicit scheme is different from the AB2 semi-implicit scheme. Here, the update of the baroclinic velocity at $t = n + 1/2$ is crucial since the vertical velocity is calculated at this intermediate time step. For

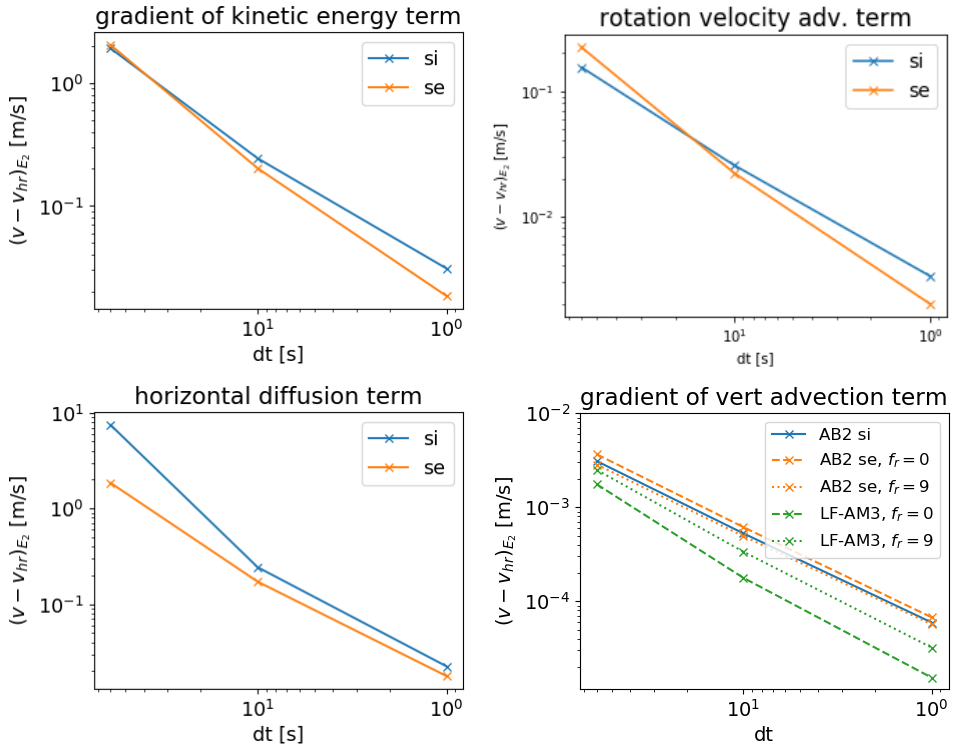

Figure 4.2: E_2 norm for diagnostic experiments which use only the isolated slow changing terms of the right-hand side as the driving dynamic for different time step sizes.

the AB2 split-explicit scheme we see a smaller error with a large filter width $f_r = 9$ compared to a smaller filter-width $f_r = 0$. In comparison, for the LF-AM3 scheme, we see a larger error for the same larger filter.

We assume that this is due to the coupling error that we discussed previously 3.7.3. The centroid position of the secondary filter for $f_r = 0$ is at $t = n + 0.5125$ and for $f_r = 9$ at $t = n + 0.7$. Hence, for the LF-AM3 scheme, for which we predict the baroclinic velocity to be at $n + 1/2$, this error of the update becomes smaller since the centroid position of the secondary filter is closer to $t = n + 1/2$. For the AB2 schemes however, the velocity is interpolated to $t = n + 0.6$. There, the secondary centroid position is similarly far away from the interpolated velocity. The vertical velocity is calculated at $n + 1/2$ and needed for the vertical advection which is the only dynamic in this test. We guess that the error becomes larger for a smaller filter width since the AB2 scheme is more unstable if the intermediate velocity is centered at $t = n + 1/2$ as we discussed in section 3.2. Hence, the filter which centers the barotropic dynamics closer to $n + 1/2$ shows a slightly larger error than the filter which centers the barotropic dynamics right of $t = n + 0.6$ with roughly the same distance from the intermediate velocity.

4.2 Gravity wave

4.2.1 Gravity wave in 1D

Similar to the tests of the slow changing terms in section 4.1.3, we test and analyse the barotropic dynamics with a 1D gravity wave test. Here, we use a toroidal grid similar to the tests in section 4.1.3 with a total longitudinal length of 640m with a triangular edge length of 4m. We use 10 vertical levels with $\Delta z_k = 10\,\mathrm{m}$. We initialize the free-surface height with a gaussian perturbation

$$\eta(x) = \exp\left(-\frac{x^2}{\sigma^2}\right), \tag{4.2.1}$$

where $\sigma = 40\,\mathrm{m}$. This gravity wave can be considered as a 1D experiment. The dynamics are only driven by the free-surface height and by the vertical integrated barotropic velocity. Within the toroidal geometry, the 2D vertical integrated velocity changes only in the latitude dimension. Hence, we consider the dynamics to be a 1D gravity wave.

Following Shchepetkin and McWilliams (2005), by neglecting the Coriolis term and with the linearization of the total depth $D = H + \eta \approx H$, one can derive the linearized barotropic equations. Over time, the gaussian perturbation splits into a right and left moving gravity wave, with both being half of the initial height after they are fully separated from each other. The nonlinearity appears in the free-surface equation (3.1.7) and the barotropic momentum equation (3.1.4). With the initial total thickness of $D = H + \eta = 100\,\mathrm{m} + 1\,\mathrm{m}$, the nonlinearity of the barotropic equation is very weak. Hence, the solution of a simulation with a small time step is similar to the analytical solution of the linearized barotropic equations. In figure 4.3 we see the evolution of the 1D gravity wave of the initial state after $2\,s$ and $4\,s$ for

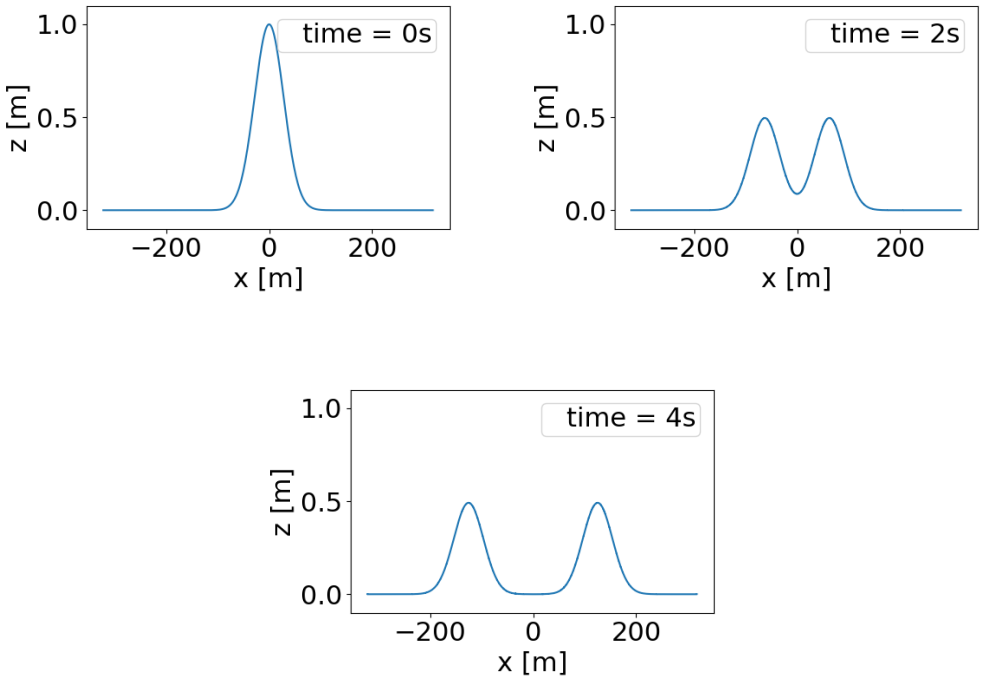

Figure 4.3: Evolution of the 1D gravity wave of the initial state (top left), after 2 s (top right) and after 4 s (bottom) for split-explicit simulation with $\Delta t = 1\,\mathrm{s}$, $M = 0$ barotropic steps and the smallest rectangular filter $f_g = 0$.

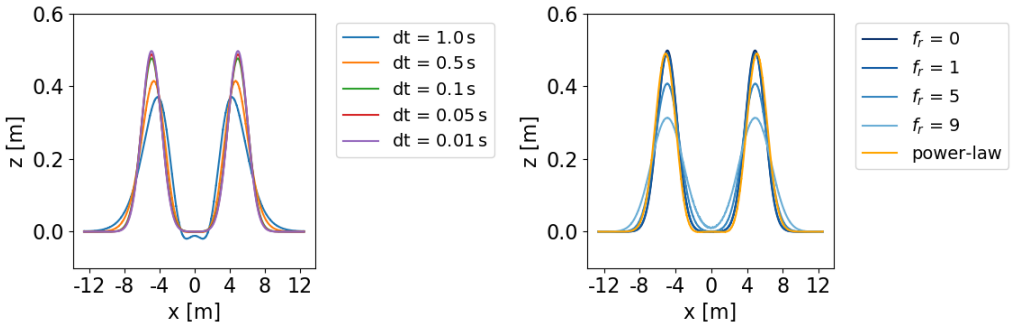

Figure 4.4: 1D gravity wave after 4s. Left of the AB2 semi-implicit time-stepping scheme with varying time-step sizes and right of the LF-AM3 split-explicit scheme for with varying rectangular filter width f_r and with the power-law filter for the time-step size $\Delta t = 1\,\mathrm{s}$ and $M = 10$ barotropic steps from n to n+1.

a split-explicit simulation with $\Delta t = 1\,\mathrm{s}$, $M = 0$ barotropic steps and the smallest rectangular filter $f_g = 0$ for minimal diffusion of the fast-time averaging.

On the left in figure 4.4, we see the solutions of the AB2 semi-implicit scheme with different time-steps sizes. Clearly, for large time-steps we find large diffusion. Additionally, we see a small dispersion error at large time-step sizes. On the right in figure 4.4 we show the solutions of the LF-AM3 split-explicit scheme for a simulations with the time-steps of $\Delta t = 1$ s and $M = 10$ barotropic substeps between n and $n + 1$. In different simulations, we use either the rectangular filter, or the power-law filter. For the rectangular filters we find stronger diffusion for larger filter width up to where we subcyle up to $2M - 1$ for $M = 9$. The power-law filter results in a small phase-error. However, its diffusion is roughly as small as for the rectangular filter with $f_g = 1$. These results are comparable to Shchepetkin and McWilliams (2005), where the properties of different filter shapes are calculated analytically.

In figure 4.5 we show the maximum norm $E_{\max}$ of the AB2 semi-implicit scheme and the LF-AM3 split-explicit scheme after 4s. We compare the $E_{\max}$ norm for a baroclinic time-step of the semi-implicit scheme with the relative barotropic time-step of the split-explicit scheme. The high resolution simulation is calculated with the semi-implicit scheme with $\Delta t = 0.001\,\mathrm{s}$. For the split-explicit simulations we choose baroclinic time-steps of 1 s and 4 s with varying numbers of barotropic time-steps M. For the LF-AM3 split-explicit scheme, we use the most precise rectangular filter with the filter width $f_r = 0$. Here, by using a baroclinic time step of 4s for LF-AM3, only one barotropic subcycle is calculated. For $f_r = 0$, the only nonzero coefficient of the primary filter is the coefficient of the last barotropic time-step M. Hence, the final result of the free-surface height is equals to the solution of the final barotropic time-step without fast-time averaging.

Overall, we see that the AB3-AM4 algorithm that we chose for the barotropic stepping is more than one order of magnitude more precise for this gravity wave than the AB2 semi-implicit scheme, even under consideration that we compare the size of the barotropic time-step of the LF-AM3 split-explicit scheme with the size of the baroclinic time-step of the semi-implicit scheme. However, this is expected, since

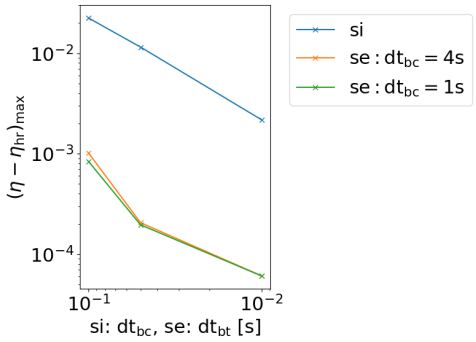

Figure 4.5: $E_{\max}$ norm of the AB2-semi-implicit scheme and the LF-AM3 split-explicit scheme for the 1D gravity wave experiment. The x-axis is the baroclinic time step of the AB2 semi-implicit scheme and the relativ barotropic time-step of the LF-AM3 split-explicit scheme.

the two-step AB3-AM4 scheme which is used to solve the barotropic system for the split-explicit schemes is expected to be more accurate compared to the implicit solution of the free-surface height of the AB2 semi-implicit scheme for such a strong gravity wave. Additionally, we see a slightly larger error for the split-explicit scheme with $\Delta t = 4\,\mathrm{s}$ where only one barotropic subcycle is calculated compared to the solution of the split-explicit scheme with $\Delta t = 1\,\mathrm{s}$ where 4 barotropic subcylces are calculated. We emphasis, that for $f_g = 0$, the solution of the primary filter is equals to the solution of the last barotropic time-step and the result of the primary filter is not time-averaged. Hence, the barotropic solution is not damped due to this primary filter. The split-explicit time-stepping scheme can become unstable due to too large gradients of the free-surface height at the beginning of the experiment. As described in section 3.5, we use an Euler step for the first time-step of the barotropic subcycling and a reduced form of the AB3-AM4 scheme for the second barotropic time-step. Both are more dissipative than AB3-AM4. We guess that this additional dissipation due to a more often occurring initialization phase for the split-explicit simulation with $\Delta t = 1\,\mathrm{s}$ stabilizes these large gradients (for large Δt) in this gravity wave experiment and results in slightly smaller error.

4.2.2 Gravity wave on an aqua planet

In this section, we analyse a gravity wave similar to the one discussed in the previous section 4.2.1, However, we simulate this time on a 3D mirrored aqua planet with a grid size of 316 km. Also, we not only solve the barotropic subsystem but the full right-hand side of the momentum equation. This is also a test for a non-uniform horizontal grid. Besides this experiment, all other experiments are of reduced spatial dimension and without the Coriolis force. In this 3D experiment, we can test the new split-explicit scheme, for dynamics for which the Coriolis force plays a role. This is of particular interest since the Coriolis force is a part of the fast changing barotropic terms (see also equation (3.1.4)) which we solve during the barotropic subcycling. Again, we initialize the free-surface with the gaussian function (4.2.1). Here, x is to be considered as the distance from the center in degrees in 2D and $\sigma = 20°$ which results in a 2D gaussian blob.

The evolution of the gravity wave for a high-resolution run of the LF-AM3 split-explicit scheme with time step of $\Delta t = 2\,\mathrm{m}$ is shown in figure 4.6 for the initial state, after 5 days and after 10 days.

In the previous section, where we excluded the Coriolis force, the initial gaussian free-surface splits in a left and in a right moving wave. Here, as shown in figure 4.6, the Coriolis force leads to structures which are symmetric in the equator. In figure 4.7 we compare the E_2 norm of the semi-implicit scheme with the new LF-AM3 split-explicit scheme after 10 days for decreasing time-step size. For the split-explicit scheme, we use M=30 barotropic step and the least dissipative rectangular filter size $f_r = 0$. The experiment is mainly driven by barotropic dynamics. We find that the split-explicit scheme is more than two orders of magnitude more accurate than the semi-implicit scheme in this experiment. We argue that this is due to the much smaller barotropic time-step for the split-explicit scheme in addition to the higher precision of the AB3-AM4 barotropic time step as shown in section 4.2.1.

The new split-explicit space-time discretization is as expected more accurate than the old semi-implicit discretization for the mainly barotropic gravity-wave experiments in the previous section and in this section. Hence, the new discretization of the barotropic system in section 3.5 works also in a 3D geometry which includes the Coriolis force and can be more accurate for these dynamics than the old semi-implicit discretization.

4.2.3 Gravity wave in 2D over an ocean mound

We have tested and analysed the barotropic dynamics in the previous two section. In this experiment, we add an ocean mound with a steep boundary to a 2D gravity wave, to cause a significant barotropic-baroclinic coupling.

For this experiment, we initialize a gravity wave on a toroidal grid, similar to section 4.2.1. The grid has a total width of 158km and an edge length of 3.16km. We use 10 vertical layers, each $\Delta z_k = 10\,\mathrm{m}$. Additionally, we add a steep ocean mound as can be seen in grey in figure 4.8. There, we show the evolution of the free-surface height in the left column and of the lateral velocity in the right column for the initial time step, after 30 min and after 60 min by using the new LF-AM3 split-explicit scheme with a time step of $\Delta t = 0.01\,\mathrm{s}$, $M = 30$ barotropic steps and a filter width of $f_r = 0$. This is the high resolution simulation for the analysis of the error norms. The largest stable time step for the AB2 semi-implicit scheme is 14 s, for the AB2 split-explicit scheme with $M = 30$ and $f_r = 0$ it is 12 s and for the LF-AM3 split-explicit scheme with M=30 and $f_r = 0$ it is 17 s.

For both split-explicit schemes, we can increase the stability by increasing the rectangular filter size to $f_r = 29$. Then, for the new LF-AM3 split-explicit scheme, the maximum time-step is $19s$ and for the AB2 split-explicit scheme it is 14 s, equal to the AB2 semi-implicit scheme. With this the maximum possible time-step is roughly 1.3 times larger for the LF-AM3 scheme compared to both AB2 schemes.

In figure 4.10 we show the E_2 norm of the free-surface height on the left and of the lateral horizontal velocity on the right. The E_2 error of both new split-explicit time-stepping schemes is of an order of magnitude smaller compared to the AB2 semi-implicit scheme. The steep initial gravity wave causes strong barotropic dynamics at

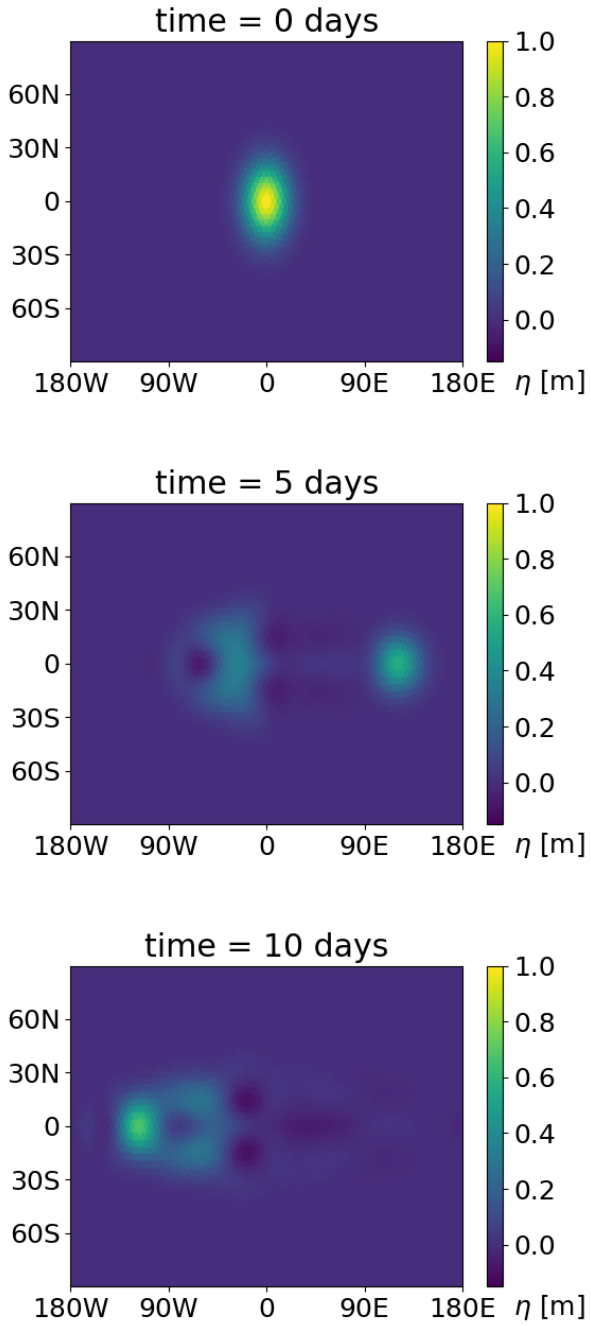

Figure 4.6: Evolution of the 3D gravity wave for the initial time-step (top row), after 5 days (middle row) and after 10 days (bottom row).

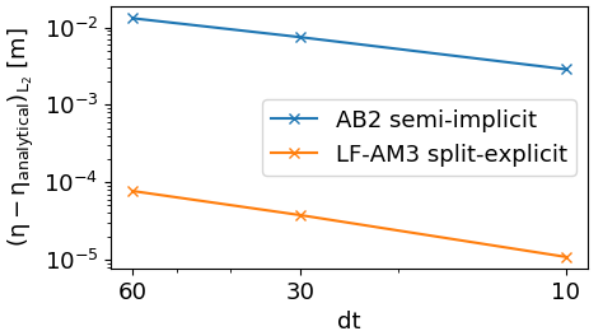

Figure 4.7: E_2 error norm of the free-surface height of the 3D gravity wave test after 10 days.

the beginning of the simulation, which the split-explicit time-stepping schemes solve more accurate due to the subcycling. We show in an example of the AB2 split-explicit scheme with the more dissipative large rectangular filter $f_r = 29$, that the dissipation of such filter can be even larger than the dissipation of the semi-implicit scheme, as the error is slightly larger. Still, the stability and therefore the maximum possible time step does not increase compared to the semi-implicit scheme.

We find, that although the simulations become unstable for large time steps, the Courant numbers are below 10^{-2} and the CFL criterion is not violated. We associate the arising instabilities to non-barotropic noise on the grid scale as can be seen for the largest time-step of the AB2 semi-implicit scheme in the upper panel of figure 4.9. Since the noise is non-barotropic, it cannot be damped with larger diffusion during the barotropic subcycling of the new split-explicit schemes. We guess, that the instabilities appear due to large gradients within the baroclinic velocity.

With this experiment, we have shown that, besides the barotropic dynamics, the new split-explicit space-time discretizations do calculate the barotropic-baroclinic coupling accurately. The stability of space-time discretizations is not only dependent on the CFL criterion, but also on the dynamics within the coupled system (Lemarié et al., 2015). In this experiment where the stability of the discretizations is not limited by the CFL criterion, the new LF-AM3 split-explicit scheme shows a larger stability in terms of an 1.3 times increased maximum time-step compared to both AB2 schemes.

4.3 Lock-exchange

After testing barotropic and baroclinic dynamics in the previous sections, in this section, we include and analyse tracers with the lock-exchange test (Ilicak et al., 2012). We follow the experiment setup of Ilicak et al. (2012) and Petersen et al. (2015). Again, the experiment is in 2D (x,z), this time in a channel geometry. The solid walls are on the left and right of the x-coordinate, and we use again periodic boundaries in the y direction, in which the values are considered to be constant. The domain size of the grid is 64 km, and the edge length of the triangles 500 m. The

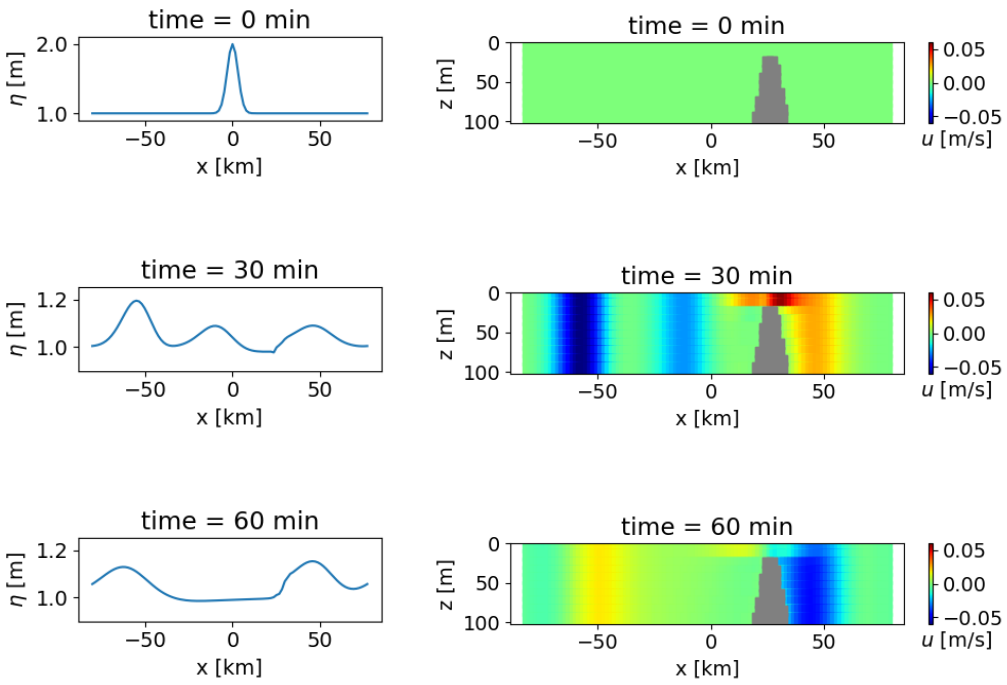

Figure 4.8: Evolution of the 2D gravity wave for the initial time-step and after 20 minutes and 40 minutes with the LF-AM3 split-explicit scheme and $\Delta t = 0.01\,\mathrm{s}$ defining the high resolution run.

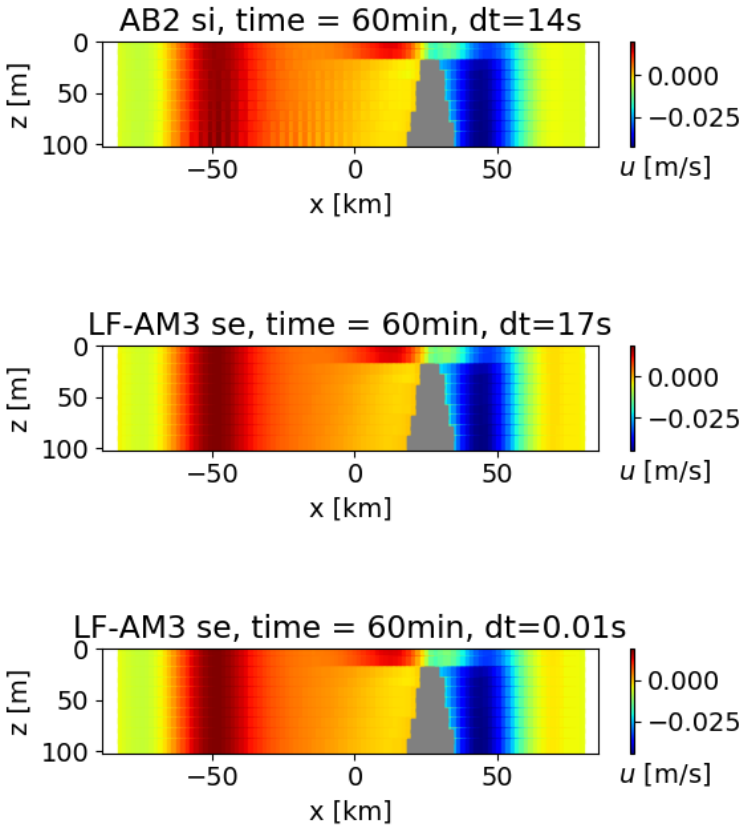

Figure 4.9: Comparison between the highest stable time step size of the semi-implicit scheme, the split-explicit scheme and the high-resolution (small time-step $\Delta t = 0.01\,\mathrm{s}$) run. Compared to figure 4.8, the axis are rescaled to see the differences between the simulations better

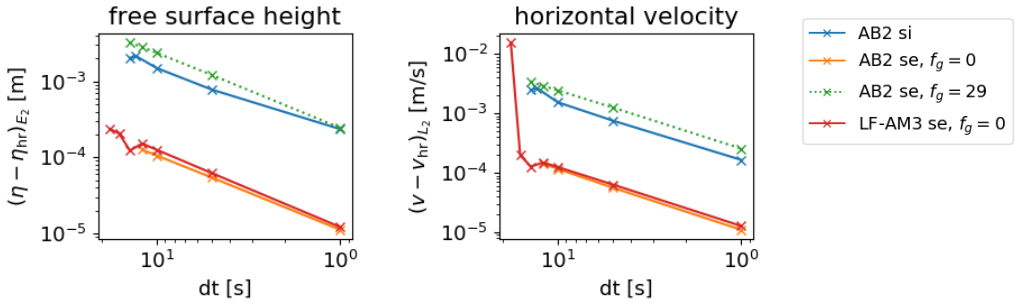

Figure 4.10: E_2 error norm of the free surface height (left) and the longitudinal velocity.

only non-uniform initial variable is the temperature with $5°C$ in the left half of the domain and $30°C$ in the right half of the domain. The initial temperature can be seen in the top panel of figure 4.6. The initial velocity and free-surface height are zero. To calculate density, we use a linearized equation of state which is

$$\rho(T, S) = \rho_0 - \alpha(\rho - \rho_0) + \beta(S - S_0) \tag{4.3.1}$$

Here, $\rho_0 = 1000\,\mathrm{kg\,m^{-3}}$, $\alpha = 0.2\,\mathrm{kg\,m^{-3}}$ and $T_0 = 5°C$. With an initial uniform salinity field $S = S_0$, the salinity does not change throughout the experiment. The vertical velocity coefficient is $\mathbb{A}^{\mathbf{v}} = 0.0001\,m^2/s$. As in the previous experiments, no forcing is applied on the boundaries or fluxes. Additionally, since the experiment is in 2D, no Coriolis force is used.

For this experiment, we use two different vertical resolutions, a high resolution with 20 vertical levels, with $\Delta z_k = 1\,\mathrm{m}$ and a new low resolution with 6 vertical levels, with $\Delta z_k = 3.3\,\mathrm{m}$. The high-resolution setup is used in Ilicak et al. (2012) and Petersen et al. (2015). For the high-resolution setup, the stability of the simulations is limited by the vertical CFL criterion. However, the LF-AM3 scheme is developed especially for high stability and accuracy for large horizontal Courant numbers, which only reflects the stability in the horizontal direction. For the low resolution configuration, the vertical Courant number becomes smaller, larger time step sizes are possible, and the stability is limited to the horizontal CFL criterion. Hence, we can use the high resolution configuration to compare the different time-stepping schemes for low horizontal Courant numbers and the low resolution configuration for large and limiting horizontal Courant numbers. Further, the low resolution configuration with high horizontal Courant numbers describes the horizontal Courant numbers in which ocean models typically run.

The initial condition of the temperature of the lock-exchange experiment can be seen in the top row of figure 4.11. Over time, the boundary of the temperature tilts so that the warmer and less dense water flows to the left over the cold, denser water which flows to the right. With zero tracer diffusion, the ideal result would be no mixing of the temperature as can be seen in isopycnal models (Ilicak et al., 2012; Petersen et al., 2015).

For our z-coordinate model, we show the state of the temperature after 16 hours for the AB2 semi-implicit scheme and the LF-AM3 split-explicit scheme for two different lateral velocity diffusion parameters $\mathcal{D}_h = 100\,\mathrm{m^2/s}$ and $\mathcal{D}_h = 1\,\mathrm{m^2/s}$ in figure 4.6, which are also used in Ilicak et al. (2012) and Petersen et al. (2015).

For this model setup, we find that for high-viscosity simulations, hardly any mixing occurs, whereas strong mixing occurs for the low viscous configuration which is the expected outcome of such setup (Ilicak et al., 2012; Petersen et al., 2015). This is due to grid scale noise in the velocity field which results in larger diapycnal mixing of tracers (Griffies and Hallberg, 2000; Ilicak et al., 2012). In this lock-exchange experiment, this grid-scale noise is mainly caused by noise in the divergence of the horizontal velocity field due to large energy of the horizontal velocity on small scales (Ilicak et al., 2012). This causes noise in the vertical velocity and increased mixing (Ilicak et al., 2012). Increasing the horizontal velocity diffusion flattens

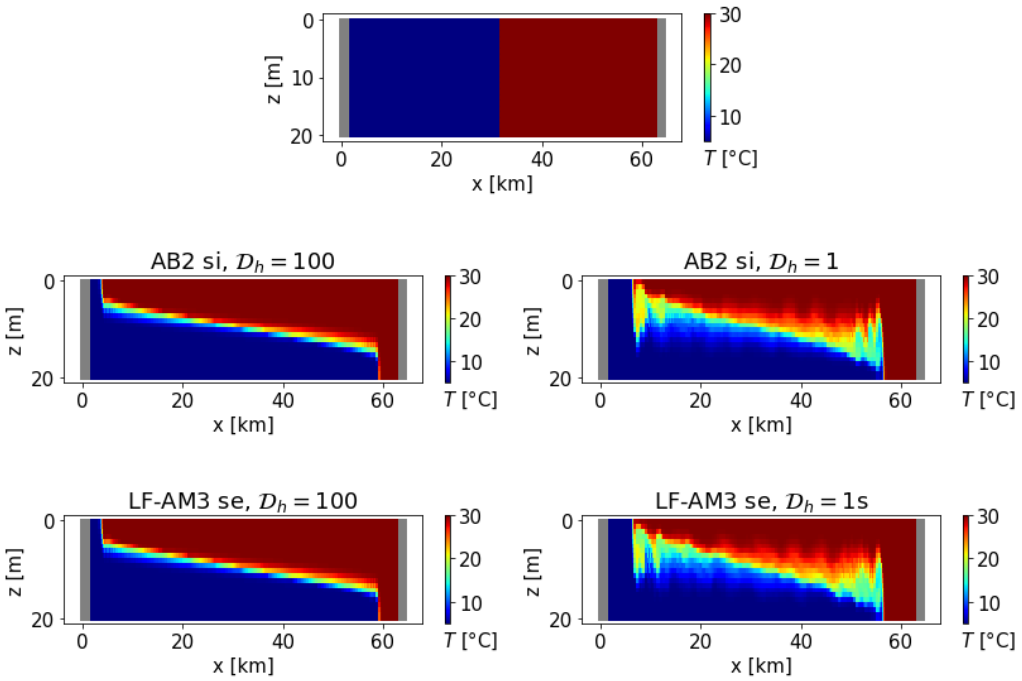

Figure 4.11: Temperature of the lock-exchange test after 16h for the semi-implicit scheme (middle row) and the LF-AM3 split-explicit scheme (bottom row) with a baroclinic time step of $\Delta t = 30\,\mathrm{s}$ and the horizontal velocity diffusion $\mathcal{D}_h = 100\mathrm{m}^2/\mathrm{s}$ (left column) and $\mathcal{D}_h = 100\mathrm{m}^2/\mathrm{s}$ (right column). The top row shows the initial state of the temperature.

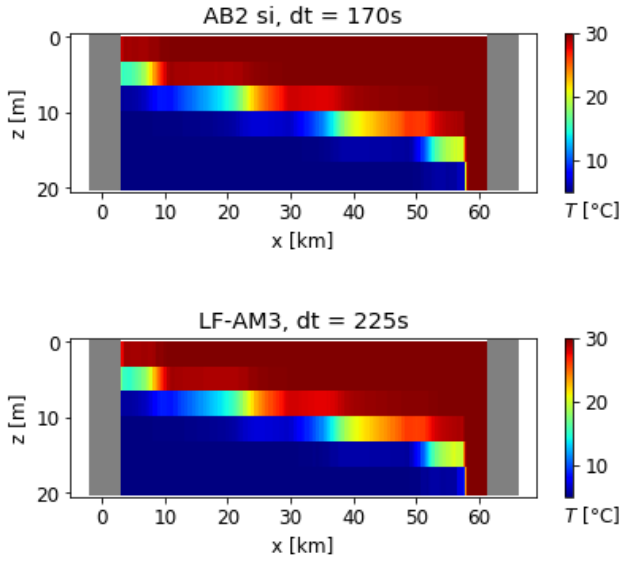

Figure 4.12: Lock-exchange test with only 4 vertical layers with high velocity viscosity $v_h = 100 m^2/s$ at 16h for the AB2 semi-implicit scheme with $\Delta t = 170\,\mathrm{s}$ and the LF-AM3 split-explicit scheme with $\Delta t = 225\,\mathrm{s}$. Both schemes use the maximal stable time-step.

the noise in the horizontal velocity and as such decreases spurious mixing. ROMS for example uses a third-order, upstream-biased dissipative advection scheme for momentum transport (Shchepetkin and McWilliams, 2005). For the lock-exchange experiment, ROMS shows less diapycnal mixing than comparable non-isopycnal models which is associated with the build-in dissipation within the momentum advection of ROMS (Ilicak et al., 2012; Petersen et al., 2015). Hence, for the later discussion of the comparison of the time-stepping schemes, we want to emphasise that in this experiment, smaller diffusion of the velocity causes larger diapycnal mixing.

As described earlier, for the simulations with low vertical resolution, we can analyse the maximum possible horizontal Courant numbers. For this coarse vertical resolution, we show the temperature after 16 hours in figure 4.12 for the largest stable time step of the AB2 semi-implicit discretization which is $\Delta t_{\max} = 170\,\mathrm{s}$ and for the largest stable time step of the new LF-AM3 split-explicit discretization which is $\Delta t_{\max} = 225\,\mathrm{s}$. The largest stable time step for the AB2 split-explicit scheme is $\Delta t_{\max} = 150\,\mathrm{s}$.

With that, the largest time step for the LF-AM3 scheme is roughly 1.3 times larger than for the AB2 semi-implicit scheme and roughly 1.5 times larger than for the AB2 split-explicit scheme. The Courant numbers are 0.43 for the new LF-AM3 split-explicit scheme, 0.33 for the old AB2 semi-implicit scheme and 0.27 for the new AB2 split-explicit scheme.

For the following analysis, we analyse the lock-exchange experiment for both vertical resolutions for high velocity diffusion $v_h = 100\,\mathrm{m}^2/\mathrm{s}$. This high velocity diffusion is recommended for this experiment to avoid most of the spurious mixing (Ilicak et al.,

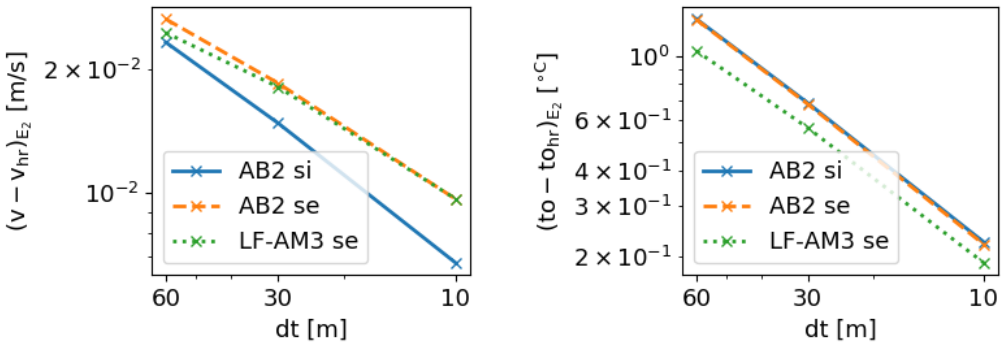

Figure 4.13: E2 error norm of the horizontal velocity (left) and the temperature (right) for the high resolution simulation with 20 vertical layers with at time-step size of $\Delta t = 30\,\mathrm{s}$ for the AB2 semi-implicit scheme, the AB2 split-explicit scheme and the LF-AM3 split-explicit scheme.

2012). For the analysis of both new split-explicit schemes, we use $M = 20$ barotropic time steps and the largest rectangular filter width $f_r = 19$.

We show the E_2 error norm of the horizontal velocity and the temperature of the high resolution configuration in figure 4.13 and of the low resolution configuration in figure 4.14 for the new LF-AM3 split-explicit scheme, the new AB2 split-explicit scheme and the old AB2 semi-implicit scheme. To calculate the E_2 error norm, we use a high resolution simulation of the AB2 semi-implicit scheme with a time step of $\Delta t = 1\,\mathrm{s}$.

For all simulations, the error converges to a simulation of the AB2 semi-implicit scheme with a time step of $\Delta t = 1\,\mathrm{s}$ in both, velocity and temperature. However, for the high vertical resolution configuration, we find that the AB2 semi-implicit scheme shows a smaller error in the velocity compared to both split-explicit schemes. There, both split-explicit schemes have nearly the same larger error despite the maximum time step of $\Delta t = 60\,s$. The E_2 error of the temperature is smaller for the new LF-AM3 scheme compared to both AB2 schemes.

For the coarse vertical resolution, the new LF-AM3 scheme has a similar smaller error in the temperature compared to both AB2 schemes. In the velocity, the error of the LF-AM3 scheme is smaller for the largest stable time step of $\Delta t_{max} = 225\,\mathrm{s}$ than the error in the velocity for both AB2 schemes for their respectively largest stable time steps. For smaller time steps, the error of the velocity of the LF-AM3 scheme approaches the error of the AB2 split explicit scheme. The AB2 split-explicit scheme has a larger error in the velocity and a smaller error convergence compared to the AB2 semi-implicit scheme.

We argue, that for small time steps used in the coarse resolution configuration, the convergence of the error in the velocity of both split-explicit schemes is comparable to the high resolution configuration. In the high resolution configuration low horizontal Courant numbers are used. In this experiment, the representation of the barotropic mode is not crucial. That is why Ilicak et al. (2012) use a barotropic time step equal to the baroclinic time step. Hence, especially for small Courant numbers, the AB2

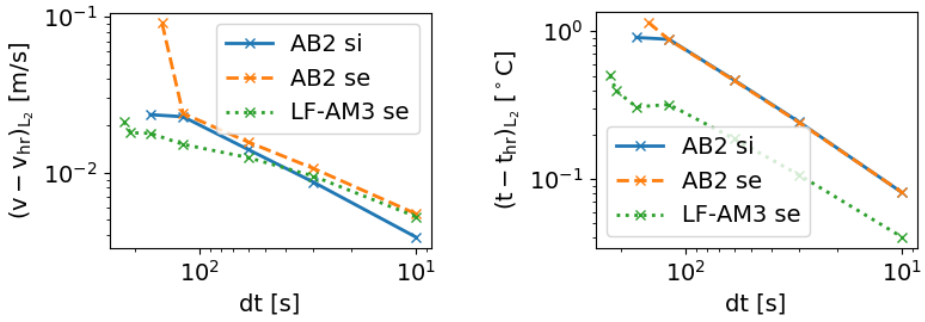

Figure 4.14: E_2 norm of the lock-exchange for the velocity (left) and the temperature (right) for the low resolution configuration with only 6 vertical layers for the AB2 semi-implicit scheme, the AB2 split-explicit scheme and the LF-AM3 split-explicit scheme for different time step sizes.

semi-implicit scheme is also highly accurate regarding the barotropic representation. There, the coupling error which is discussed in section 3.7.3 causes the large error within the velocity of both split-explicit schemes.

For large Courant numbers, the accuracy of the dominant baroclinic dynamics is the major error source. Accordingly, the error of the velocity of both AB2 schemes, which use the same baroclinic step, is similar. For large Courant numbers, the new LF-AM3 scheme shows higher stability and higher accuracy in the velocity then both AB2 schemes.

In comparison to the error of the velocity, the E_2 error in the temperature is smaller for the LF-AM3 scheme compared to both AB2 schemes for all time steps and for both vertical resolutions. Temperature is transported with the velocity at the intermediate time step $n + 1/2$. For the LF-AM3 scheme the velocity at $n + 1/2$ that transports the tracers is interpolated with a large stencil including the predicted velocity at $n + 1/2$. For the AB2 schemes the weighted velocity is interpolated from the values at n and $n + 1$ which is less accurate.

The higher accuracy in the temperature of the LF-AM3 scheme compared to both AB2 schemes can also be seen in the analysis of the RPE. In figure 4.15, we compare the RPE from the AB2 semi-implicit scheme with the LF-AM3 split-explicit scheme for different time step sizes. The normalized RPE of both schemes increases over time comparable to the analysis in Ilicak et al. (2012) and Petersen et al. (2015). For both schemes, the normalized RPE increases with decreasing time step and converges to the RPE of the AB2 semi-implicit scheme with the smallest time step of $\Delta t = 1\,\mathrm{s}$ (solid orange line). Additionally, for the same time step size, the normalized RPE of LF-AM3 scheme is larger than the AB2 semi-implicit scheme. Hence, the spurious mixing is larger for smaller time steps and of the new LF-AM3 scheme compared to the AB2 semi-implicit scheme.

As we discussed earlier, a decrease of velocity diffusion results in an increase of spurious mixing in this experiment. The total velocity diffusion can be considered as a sum of the physical velocity diffusion and the numerical diffusion. The numerical

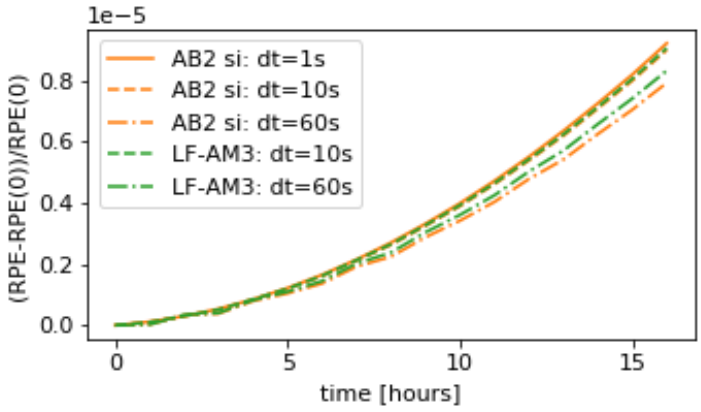

Figure 4.15: Evolution of the reference potential energy (RPE) over time of the lock-exchange experiment in the high resolution configuration with 20 vertical layers for the AB2 semi-implicit scheme and the LF-AM3 split-explicit scheme for different time-step sizes and with the horizontal velocity diffusion $\mathcal{D}_h = 100\,\mathrm{m}^2/\mathrm{s}$.

diffusion of momentum decreases with decreasing time step size. Hence, the total diffusion decreases with decreasing time step size and the spurious mixing and therefore the normalized RPE increases.

We show this in more detail in figure 4.16 around the last time step at $t = 16\,\mathrm{h}$. There we show additionally the normalized RPE of the AB2 split-explicit scheme and the normalized RPE of LF-AM3 scheme where we use the higher-accurate power-law filter. The AB2 split-explicit scheme (red) has a slightly smaller RPE than the AB2 semi-implicit scheme (orange) for each respective time step. The interpolation of the intermediate velocity is similar for both schemes, but the coupling error of the barotropic mode causes a diffusion which decreases the normalized RPE. LF-AM3 show a larger RPE with the power-law filter (purple) compared to the rectangular filter (green). The power-law filter is less diffusive than the large rectangular filter. Additionally, the centroid position is closer to the intermediate velocity which reduces the coupling error. Therefore, the result of the power-law filter is less diffusive and the spurious mixing is increased.

As a complementary analysis, we show the normalized RPE for the coarse vertical resolution in figure 4.17. Here, the RPE of both schemes also converges to a larger RPE with decreasing time step size. In particular, the RPE of the split-explicit scheme with a large time step of $\Delta t = 120\,\mathrm{s}$ is even comparable to the semi-implicit scheme with a time step of $\Delta t = 10\,\mathrm{s}$.

In this section, we analysed accuracy, diapycnal mixing and stability for the lock-exchange experiment where temperature as a tracer variable is included. We found that for low horizontal Courant numbers, a coupling error of the split-explicit schemes results in a larger error in the velocity compared to the AB2 semi-implicit schemes. This coupling error becomes becomes smaller for relevant large Courant numbers. There, the new LF-AM3 split-explicit scheme is more accurate in the velocity compared to both AB2 schemes. Additionally, the LF-AM3 scheme is more accurate regarding the temperature for all time steps sizes.

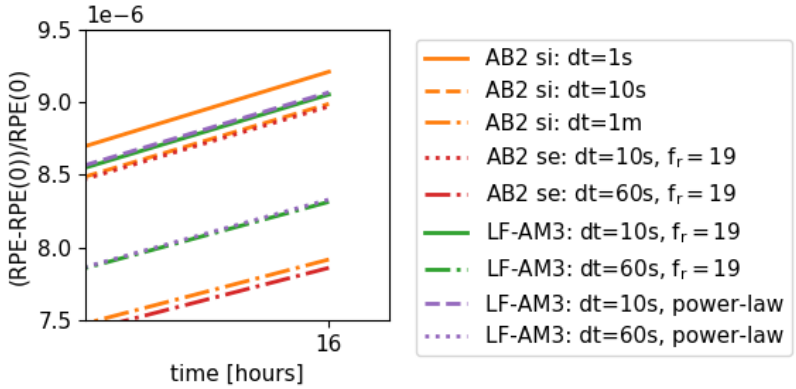

Figure 4.16: Change of RPE at t=16h of the lock-exchange experiment in the high-resolution configuration with 20 vertical layers for different time steps of the AB2 semi-implicit scheme, the AB2 split-explicit scheme and the LF-AM3 split-explicit scheme with the horizontal velocity diffusion $\mathcal{D}_h = 100\,\mathrm{m}^2/\mathrm{s}$. For the split-explicit schemes, simulations are shown using $M = 20$ barotropic steps between n and $n+1$ using the rectangular time-averaging filter with the filter width $f_r = 19$. Additionally, the power-law filter is used for the LF-AM3 split-explicit scheme.

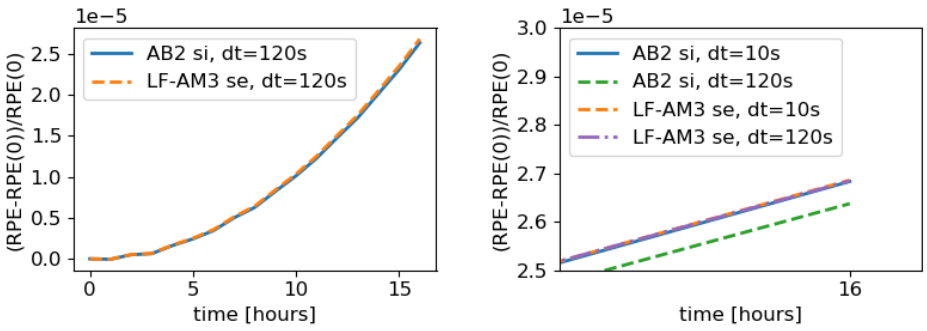

Figure 4.17: Change of RPE of the lock-exchange experiment with 6 vertical layers for the AB3 semi-implicit scheme and the LF-AM3 split-explicit scheme for $\Delta t = 10\,\mathrm{s}$ and $\Delta t = 120\,\mathrm{s}$. Except for the AB2 semi-implicit scheme with $\Delta t = 120\,\mathrm{s}$, the RPE is nearly the same for the other configurations and the lines overlap.

We find larger normalized RPE for decreasing time step sizes and for the new LF-AM3 space-time discretization compared to both the new split-explicit AB2 scheme and the old semi-implicit AB2 scheme. We argue that this is due to smaller numerical diffusion of the time-stepping in particular within the intermediate time step. Smaller numerical diffusion results in noise of the velocity on small grid-scales and thus in larger spurious mixing.

For the lock-exchange experiment, we find that the CFL limit of the new LF-AM3 space-time discretization is of a factor 1.3 larger than the CFL limit of both AB2 discretizations.

4.4 Overflow

In a final experiment, we qualitatively compare the solution of the overflow test case (Ilicak et al., 2012; Petersen et al., 2015). This experiment is similar to the lock-exchange experiment but additionaly includes bathymetry. In figure 4.18 we show the initial temperature (top row) as well as the temperature after 6 hours for the AB2 semi-implicit scheme (middle row) and the new LF-AM3 split-explicit scheme (bottom row). In the left column, we show the results of both schemes with high velocity diffusion of $\mathcal{D}_h = 1.0 \cdot 10^4\,\mathrm{m}^2/\mathrm{s}$ and in the right column for small velocity diffusion $\mathcal{D}_h = 1\,\mathrm{m}^2/\mathrm{s}$. In this experiment, the dense cold water ideally flows downwards along the slope without mixing. This overflow experiment is ideal to test diapycnal mixing for terrain-following or similar vertical coordinates. Compared to these vertical coordinate systems, z-coordinates in particular show large mixing. For z-coordinates, the resolution along the ideal flow is low compared to isopycnal and terrain-following coordinates and increased mixing can be seen (Ilicak et al., 2012; Petersen et al., 2015).

Still, we can treat the overflow experiment as a test for the different space-time discretizations within the z-coordinate system. For high velocity diffusion, the new LF-AM3 split-explicit scheme and the old AB2 semi-implicit scheme show a similar temperature profile after $6\,h$ simulation time, as shown in the left column of figure 4.18. However, for the low velocity diffusion simulations in the right column, we see more mixing of the LF-AM3 scheme, in particular in the right front of the cold water. This is similar to the lock-exchange experiment in the previous section 4.3. There, a decrease of numerical diffusion results in larger noise in the velocity on grid scale which causes spurious mixing.

4.5 Discussion

In the last chapter we compared and analysed the accuracy and stability of the old semi-implicit AB2 space-time discretization, the new AB2 split-explicit space-time discretization and the new LF-AM3 space-time discretization in experiments with increasing complexity.

If we separate the slow-changing terms of the right-hand side of the momentum equation (2.1.1a), the new LF-AM3 split-explicit scheme shows a similar convergence and error as both AB2 schemes. For all gravity wave tests that are highly barotropic

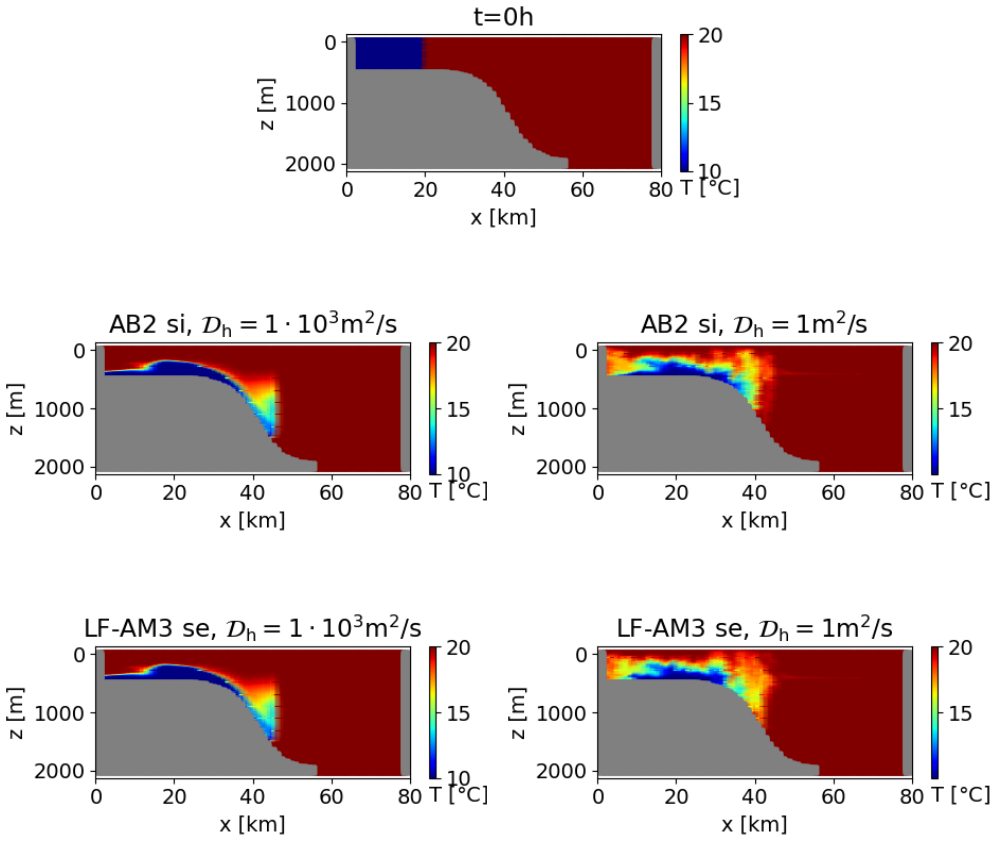

Figure 4.18: Initial temperature (top row) and temperature after 6 hours of the overflow experiment for the AB2 semi-implicit scheme (middle row) and the LF-AM3 split-explicit scheme (bottom row) for high horizontal velocity diffusion $\mathcal{D}_h = 1 \cdot 10^3\,\mathrm{m}^2/\mathrm{s}$ (left column) and low horizontal velocity diffusion $\mathcal{D}_h = 1\,\mathrm{m}^2/\mathrm{s}$ (right column).

and which may also include a 3D geometry or a bathymetry, we find that the split-explicit time-stepping schemes are much more accurate since we resolve the barotropic system with many explicit steps compared to one diffusive implicit step.

For the highly baroclinic lock-exchange experiment, we see mixed results regarding accuracy. For low lateral Courant numbers, the coupling error from the slow changing terms causes a larger error in the velocity for both split-explicit schemes. This coupling error originates from a displacement of the secondary filter weights regarding the position of the intermediate velocity as we discussed in section 3.7.3. We speculate that improved fast-time averaging filter weights, which consider the position of the intermediate velocity in addition to accuracy and convergence order, will improve these results. Even with this coupling error, for large Courant numbers, we find higher accuracy for the LF-AM3 scheme, including time step sizes that exceed the stability of the AB2 schemes. This is a desired result since ocean models usually run with the highest possible Courant numbers to reduce numerical costs.

In the lock-exchange experiment, we also analyse the reference potential energy (RPE) to measure diapycnal mixing. We find that the LF-AM3 scheme has larger normalized RPE and therefore larger mixing compared to AB2. We also find an increase in RPE and mixing for any time-stepping scheme with decreasing time step size. We argue that this is due to a less diffusive time-stepping. This results in more noise in the horizontal velocity on grid scale which causes spurious mixing and therefore an increase of normalized RPE (Griffies and Hallberg, 2000; Ilicak et al., 2012). In general, smaller diapycnal mixing is desired. However, having a smaller total diffusion caused by a reduction of the numerical diffusion in velocity can be considered as an increase of control of the total lateral velocity diffusion.

ROMS (Shchepetkin and McWilliams, 2005) achieves a lower RPE compared to models like MPAS-Ocean (Ringler et al., 2013), MITgcm Marshall et al. (1997) and MOM Griffies et al. (2010b) due to a dissipative momentum advection scheme (Ilicak et al., 2012; Petersen et al., 2015). Hence, adding diffusion in some parts of the model purposely can achieve better results regarding the diapycnal mixing due to the increase in total velocity diffusion which consists of applied velocity diffusion and numerical diffusion. The lower numerical diffusion of the new LF-AM3 space-time discretization results in the mentioned larger control of the total velocity diffusion compared to the AB2 discretization.

In addition, for the LF-AM3 split-explicit time-stepping scheme, we still use the one-step tracer scheme Korn (2017) instead of a two-step scheme that has been originally developed for the LF-AM3 scheme of Shchepetkin and McWilliams (2005). As we discussed in section 2.2.4, we chose the original 1-step tracer scheme for simplicity reasons and to be able to separately analyse changes in accuracy and stability from a change of the time discretization of the discrete momentum equation alone. With a more profound tracer scheme as well as with other more accurate high-order schemes, we expect a similarly slight increase of RPE as a sign of a decrease of total diffusion.

We could analyse the stability regarding a horizontal Courant number in the gravity wave test over an ocean mound and in the lock-exchange experiment in a new setup with coarse vertical resolution. For both experiments, the maximum possible time-step of the LF-AM3 split-explicit scheme is 1.3 times larger than for the AB2 semi-implicit schemes. Our experiments show, that the AB2 semi-implicit scheme is

generally slightly more stable than the AB2 split-explicit scheme. Accordingly for the lock-exchange test, the maximum possible time-step of the LF-AM3 scheme is 1.5 times larger than for the AB2 split-explicit scheme.

As we discussed in section 1.2, the space-time discretization has be considered for the stability of time-stepping schemes (Lemarié et al., 2015). Differences in the stability between the LF-AM3 scheme and the AB2 scheme for various space-time discretizations are analysed in Lemarié et al. (2015). For example, the CFL stability criteria of LF-AM3 for a second-order centered scheme (C2) is 1.587 and for a third-order upwind scheme (UP3) 0.871. For an AB2 scheme, the CFL limit is for C2 0.503 and for UP3 0.554 (Lemarié et al., 2015). As such LF-AM3 shows roughly a 3.2 times larger stability for C2 and 1.5 times for UP3 compared to AB2.

For the lock-exchange experiment, we find a maximum Courant number of the new LF-AM3 split-explicit discretization of 0.554, for the new AB2 split-explicit discretization 0.33 and for the AB2 semi-implicit scheme 0.43. Here, LF-AM3 shows a 1.3 times larger stability than AB2 semi-implicit and 1.5 time larger than AB2 split-explicit.

We do not want to overemphasize the absolute Courant numbers. The stability of a simulation is not only dependent on a CFL limit, but also dependent on the dynamics of the system (Lemarié et al., 2015). This is comparable with the experiment of the gravity wave over an ocean mound of section 4.2.3. There, the schemes become unstable although the Courant number is below 10^{-2}. However there, LF-AM3 has an approximately 1.3 time larger possible Courant number than both AB2 schemes which is similar to the lock-exchange experiment.

This increase in stability is closer to the increase in stability of the third-order advection scheme compared to the second-order advection scheme in the analysis of Lemarié et al. (2015). In Korn (2017) it is shown that the transport scheme is similar to a second-order scheme. Also, the divergence is of second order on the torus grid that we use and which can be regarded as as a uniform planar grid. We speculate that we do achieve a smaller increase of stability with the LF-AM3 scheme compared to Lemarié et al. (2015) because of the complete spatial framework shown in Korn (2017) and that we apply for the new discretization in this thesis. Compared to the spatial framework of Lemarié et al. (2015), the framework that we use includes the unstructured icosahedral grid, first-order reconstruction operators and the mass-matrix. Still, we find an increase in stability and also accuracy of the new LF-AM3 split-explicit space-time discretization compared to the new AB2 split-explicit space-time discretization and the old AB2 semi-implicit space-time discretization.

Chapter 5

Summary and outlook

Time-stepping schemes are a crucial part of ocean circulation models. The stability and accuracy of time-stepping schemes depend highly on the underling spatial discretization (Lemarié et al., 2015). As such, the coupled space-time discretizations should be considered for the analysis of time-stepping schemes (Lemarié et al., 2015). ICON-O has a unique spatial framework as it uses a C-type staggering of variables on an icosahedral grid in combination with a mass matrix that filters out a grid mode which otherwise appears for this C-type staggering of variables on an triangular grid (Korn, 2017). Originally, an AB2 semi-implicit time-stepping is used for ICON-O (Korn, 2017).

With the aim to increase accuracy, stability and numerical efficiency we adapt a split-explicit time-stepping scheme based on a LF-AM3 baroclinic step which was developed for ROMS in Shchepetkin and McWilliams (2005) and Shchepetkin and McWilliams (2009) for the mathematical framework of ICON-O. This results in a new split-explicit space-time discretization which uses C-type staggering on a triangular grid. While ROMS has a two-step tracer scheme, we apply the time-stepping scheme for the original one-step tracer scheme of ICON-O. The new split-explicit time-stepping discretization fulfills volume and tracer conservation. Within the new split-explicit discretization, we preserve the mass-matrix which filters out the spurious mode within the continuity equation (Korn, 2017). Additionally, we adapted the split-explicit time-stepping for the original AB2 baroclinic step.

In subsequent steps, we tested and analysed the new split-explicit time-stepping schemes and compare them to the original AB2 semi-implicit scheme. In several highly barotropic gravity wave experiments in different geometries, we find that the new split-explicit schemes are much more accurate than the semi-implicit scheme for the same baroclinic time step. Further, the split-explicit schemes are still more accurate, if the same barotropic time step is used as in the AB2 semi-implicit scheme. We find that, depending on the number of barotropic steps and on the fast-time averaging filter which is applied over the barotropic solution, we can reduce the error of the barotropic system by orders of magnitude. Such more accurate and less diffusive representation of the propagation of barotropic signals is highly desirable for global ocean models, e.g. when investigating the interaction of barotropic tides with the general circulation (e.g. Li and Storch (2020)).

We conducted a lock-exchange experiment for a quantitative analysis of accuracy and

stability for baroclinic dynamics and tracer properties. For low Courant numbers, a coupling error, which is based on a shift between the position of the intermediate baroclinic velocity and the result of the secondary filter-weights, results in lower accuracy compared to the AB2 semi-implicit scheme. We argue that this error can be resolved with new filters which respect the centroid condition of the secondary filter-weights at $n + 1/2$ for the LF-AM3 scheme or with filters which respect the interpolated position at $n + 0.6$ for the AB2 scheme. We define a new low vertical resolution of the lock-exchange experiment to analyse accuracy and stability for high Courant numbers. Results for such high Courant numbers near the CFL limit are of particular interest since ocean models are usually run with large time steps near the CFL limit to decrease numerical costs. For these high Courant numbers, the coupling error becomes relatively small as we see from a comparison between the new AB2 split-explicit time-stepping scheme and its semi-implicit version in figure 4.14.

Moreover in the lock-exchange experiment, for large Courant numbers, the new LF-AM3 scheme has an increased accuracy compared to both AB2 schemes even beyond the stability of the AB2 schemes. Additionally, due to a more accurate representation of the intermediate velocity, we find that tracers are calculated more accurately for all time step sizes with the new LF-AM3 scheme. This slightly increases the tracer mixing. We suggest that this is due to a decrease of the numerical diffusion of the velocity as a result of the more accurate LF-AM3 scheme, in particular at the intermediate time step. This decrease of numerical diffusion results in larger noise of the velocity on grid scale which causes an increase of spurious mixing (Griffies and Hallberg, 2000; Ilicak et al., 2012). A decrease of numerical diffusion gives an increase of control over the total velocity diffusion. This can be especially beneficial for example for high resolution experiments where small velocity diffusion is used.

We find in our experiments that the maximum possible Courant numbers of LF-AM3 split-explicit scheme is 1.3 times larger compared to the AB2 semi-implicit scheme and up to 1.5 times larger than the AB2 split-explicit scheme for the lock-exchange experiment. Putting this in context of the space-time stability analysis of Lemarié et al. (2015), the increase of stability of the LF-AM3 scheme compared to the AB2 schemes is approximately as large as for their third-order upwind scheme, but smaller than for their second-order advection scheme. Although in ICON-O the transport scheme and the divergence are of second order on a torus grid (Korn, 2017), we do not achieve an increase of stability of the LF-AM3 scheme compared to the AB2 schemes as shown in Lemarié et al. (2015). We argue that this is due to differences of the overall spatial framework of ICON-O, which we use in this thesis and the spatial framework which is discussed in Lemarié et al. (2015). Such properties of the spatial framework of ICON-O are for example the icosahedral grid, first order reconstructions and the mass-matrix which filters out the grid mode (Korn, 2017). An analytical stability analysis of space-time discretizations on an icosahedral grid including the spatial framework of ICON-O similar to Lemarié et al. (2015) could be an interesting and important future contribution to the ocean model community.

Being able to use a 1.3 to 1.5 times larger time step with the new LF-AM3 split-explicit scheme compared to both AB2 schemes could result in a speedup of ICON-O and decrease the numerical costs. However, the change of numerical costs and numerical efficiency depends on many aspects of the implementation that lay outside the scope of this thesis, such as the efficiency of the parallelization. Furthermore, the

LF-AM3 split-explicit space-time discretization uses a 2-step momentum advection scheme where the right-hand side of the momentum equation is solved twice. Still, the barotropic system is only solved once as well as the implicit vertical diffusion which could lead to a decrease of numerical costs due to a larger possible time step.

For the future development of the new LF-AM3 split-explicit space-time discretization, which we derived in this thesis, the more profound two-step tracer scheme of Shchepetkin and McWilliams (2005) could be adapted. This includes changes in the Zalesak limiter (Zalesak, 1979) which is used for flux-corrected transport in ICON-O (Korn, 2017).

Further, the full parallelization of the split-explicit schemes is needed for more complex simulations such as eddy resolving or global ocean experiments. For these, also bottom and surface boundary conditions have to be considered which are not used in our idealized experiments.

Potential new experiments to test and compare the different time-stepping schemes could be following the additional experiments of Ilicak et al. (2012) and Petersen et al. (2015) where internal waves and baroclinic eddies are analysed. A further comparison of the different time-stepping schemes could be the analysis of the effective resolution which defines the range of numerical dissipation becomes dominant as discussed in Soufflet et al. (2016) for a baroclinic jet test case.

Bibliography

P. Adamidis, V. Heuveline, and F. Wilhelm. An Efficient Scalable Solver for the Global Ocean Sea-Ice Model MPIOM. *Civil-Comp Proceedings*, 95, 2011. doi: 10.4203/ccp.95.58.

A. Adcroft and J.-M. Campin. Rescaled height coordinates for accurate representation of free-surface flows in ocean circulation models. *Ocean Modelling*, 7(3):269–284, 2004. doi: 10.1016/j.ocemod.2003.09.003.

B. Bernard, G. Madec, T. Penduff, J. M. Molines, A. M. Treguier, J. Le Sommer, A. Beckmann, A. Biastoch, C. Böning, J. Dengg, C. Derval, E. Durand, S. Gulev, E. Remy, C. Talandier, S. Theetten, M. Maltrud, J. McClean, and B. De Cuevas. Impact of partial steps and momentum advection schemes in a global ocean circulation model at eddy-permitting resolution. *Ocean Dynamics*, 56(5-6):543–567, 2006. doi: 10.1007/s10236-006-0082-1.

R. Bleck and L. T. Smith. A wind-driven isopycnic coordinate model of the north and equatorial Atlantic Ocean: 1. Model development and supporting experiments. *Journal of Geophysical Research*, 95(C3):3273–3285, 1990. doi: 10.1029/jc095ic03p03273.

K. Bryan. A numerical method for the study of the circulation of the world ocean. *Journal of Computational Physics*, 4(3):347–376, 1969. doi: 10.1016/0021-9991(69)90004-7.

E. P. Chassignet, H. E. Hurlburt, O. M. Smedstad, G. R. Halliwell, A. J. Wallcraft, E. J. Metzger, B. O. Blanton, C. Lozano, D. B. Rao, P. J. Hogan, and A. Srinivasan. Generalized vertical coordinates for eddy-resolving global and coastal ocean forecasts. *Oceanography*, 19(1):118–129, 2006. doi: 10.5670/oceanog.2006.95.

T. Crueger, M. A. Giorgetta, R. Brokopf, M. Esch, S. Fiedler, C. Hohenegger, L. Kornblueh, T. Mauritsen, C. Nam, A. K. Naumann, K. Peters, S. Rast, E. Roeckner, M. Sakradzija, H. Schmidt, J. Vial, R. Vogel, and B. Stevens. ICON-A, The Atmosphere Component of the ICON Earth System Model: II. Model Evaluation. *Journal of Advances in Modeling Earth Systems*, 10(7):1638–1662, 2018. doi: 10.1029/2017MS001233.

S. Danilov. On utility of triangular C-grid type discretization for numerical modeling of large-scale ocean flows. *Ocean Dynamics*, 60(6):1361–1369, 2010. doi: 10.1007/s10236-010-0339-6.

S. Danilov. Ocean modeling on unstructured meshes. *Ocean Modelling*, 69(195-210), 2013. doi: 10.1016/j.ocemod.2013.05.005.

S. Danilov, D. Sidorenko, Q. Wang, and T. Jung. The finite-volume sea ice-Ocean model (FESOM2). *Geoscientific Model Development*, 10:765–789, 2017. doi: 10.5194/gmd-10-765-2017.

J. Demange, L. Debreu, P. Marchesiello, F. Lemarié, E. Blayo, and C. Eldred. Stability analysis of split-explicit free surface ocean models: Implication of the depth-independent barotropic mode approximation. *Journal of Computational Physics*, 398(1):108875, 2019. doi: 10.1016/j.jcp.2019.108875.

D. R. Durran. *Numerical methods for wave equations in geophysical fluid dynamics. Vol. 32.* Springer Science and Business Media, 2013. doi: 10.1007/978-1-4757-3081-4.

A. Gassmann. Inspection of hexagonal and triangular C-grid discretizations of the shallow water equations. *Journal of Computational Physics*, 230(7), 2011. doi: 10.1016/j.jcp.2011.01.014.

A. E. Gill. *Atmosphere-Ocean Dynamics*. Academic Press, 1982. ISBN 9780122835223.

M. A. Giorgetta, R. Brokopf, T. Crueger, M. Esch, S. Fiedler, J. Helmert, C. Hohenegger, L. Kornblueh, M. Köhler, E. Manzini, T. Mauritsen, C. Nam, T. Raddatz, S. Rast, D. Reinert, M. Sakradzija, H. Schmidt, R. Schneck, R. Schnur, L. Silvers, H. Wan, G. Zängl, and B. Stevens. ICON-A, the Atmosphere Component of the ICON Earth System Model: I. Model Description. *Journal of Advances in Modeling Earth Systems*, 10(7):1613–1637, 2018. doi: 10.1029/2017MS001242.

S. M. Griffies and R. W. Hallberg. Biharmonic friction with a Smagorinsky-like viscosity for use in large-scale eddy-permitting ocean models. *Monthly Weather Review*, 128(8):2935–2946, 2000. doi: 10.1175/1520-0493(2000)128⟨2935:BFWASL⟩2.0.CO;2.

S. M. Griffies, C. Böning, F. O. Bryan, E. P. Chassignet, R. Gerdes, H. Hasumi, A. Hirst, A.-M. Treguier, and D. Webb. Developments in ocean climate modelling. *Ocean Modelling*, 2(3-4):123–192, jan 2000. doi: 10.1016/S1463-5003(00)00014-7.

S. M. Griffies, A. Adcroft, H. Banks, C. W. Böning, E. Chassignet, G. Danabasoglu, S. Danilov, E. Deleersnijder, H. Drange, M. England, B. Fox-Kemper, R. Gerdes, A. Gnanadesikan, R. Greatbatch, R. Hallberg, E. Hanert, J. Harrison, S. Legg, C. Little, G. Madec, S. Marsland, M. Nikurashin, A. Priani, H. Simmons, J. Schröter, B. Samuels, A.-M. Treguier, J. Toggweiler, H. Tsujino, G. Vallis, and L. White. Problems and Prospects in Large-Scale Ocean Circulation Models. In *Proceedings of OceanObs'09: Sustained Ocean Observations and Information for Society*, volume 2, pages 437–458. European Space Agency, 2010a. doi: 10.5270/OceanObs09.cwp.38.

S. M. Griffies, M. Schmidt, and M. Herzfeld. Elements of MOM4p1. Technical report, NOAA/Geophysical Fluid Dynamics Laboratory Ocean Group, 2010b.

R. L. Higdon and R. A. de Szoeke. Barotropic-Baroclinic Time Splitting for Ocean Circulation Modeling. *Journal of Computational Physics*, 135(1):30–53, 1997. doi: 10.1006/JCPH.1997.5733.

M. Ilicak, A. J. Adcroft, S. M. Griffies, and R. W. Hallberg. Spurious dianeutral mixing and the role of momentum closure. *Ocean Modelling*, 45-46:37–58, 2012. doi: 10.1016/j.ocemod.2011.10.003.

Y. Kanarska, A. Shchepetkin, and J. C. McWilliams. Algorithm for non-hydrostatic dynamics in the Regional Oceanic Modeling System. *Ocean Modelling*, 18(3-4): 143–174, 2007. doi: 10.1016/j.ocemod.2007.04.001.

T. Kärnä Tuomas, V. Legat, and E. Deleersnijder. A baroclinic discontinuous Galerkin finite element model for coastal flows. *Ocean Modelling*, 61:1–20, 2013. doi: 10.1016/j.ocemod.2012.09.009.

P. D. Killworth, D. J. Webb, D. Stainforth, and S. M. Paterson. The Development of a Free-Surface Bryan–Cox–Semtner Ocean Model. *Journal of Physical Oceanography*, 21(9):1333–1348, 1991. doi: 10.1175/1520-0485(1991)021⟨1333:tdoafs⟩2.0.co;2.

N. V. Koldunov, V. Aizinger, N. Rakowsky, P. Scholz, D. Sidorenko, S. Danilov, and T. Jung. Scalability and some optimization of the Finite-volumE Sea ice-Ocean Model, Version 2.0 (FESOM2). *Geoscientific Model Development*, 12(9):3991–4012, 2019. doi: 10.5194/gmd-12-3991-2019.

P. Korn. Formulation of an unstructured grid model for global ocean dynamics. *Journal of Computational Physics*, 339:525–552, 2017. doi: 10.1016/j.jcp.2017.03.009.

P. Korn. A structure-preserving discretization of ocean parametrizations on unstructured grids. *Ocean Modelling*, 132:73–90, 2018. doi: 10.1016/j.ocemod.2018.10.002.

P. Korn and S. Danilov. Elementary dispersion analysis of some mimetic discretizations on triangular C-grids. *Journal of Computational Physics*, 330:156–172, 2017. doi: 10.1016/j.jcp.2016.10.059.

P. Korn and L. Linardakis. A conservative discretization of the shallow-water equations on triangular grids. *Journal of Computational Physics*, 375:871–900, 2018. doi: 10.1016/j.jcp.2018.09.002.

M. Leclair and G. Madec. A conservative leapfrog time stepping method. *Ocean Modelling*, 30(2-3):88–94, 2009. doi: 10.1016/j.ocemod.2009.06.006.

F. Lemarié. Hydrostatic CROCO time-stepping flow chart, n.d. URL `ftp://ftp.ifremer.fr/ifremer/croco/DOC/croco_step_hydro_en.pdf`. Last accessed: Sep. 28, 2020.

F. Lemarié, L. Debreu, G. Madec, J. Demange, J. Molines, and M. Honnorat. Stability constraints for oceanic numerical models: implications for the formulation of time and space discretizations. *Ocean Modelling*, 92:124–148, 2015. doi: 10.1016/J.OCEMOD.2015.06.006.

Z. Li and J. Storch. M2 Internal-Tide Generation in STORMTIDE2. *Journal of Geophysical Research: Oceans*, 125(8), 2020. doi: 10.1029/2019JC015453.

J. A. MacKinnon, Z. Zhao, C. B. Whalen, A. F. Waterhouse, D. S. Trossman, O. M. Sun, L. C. St Laurent, H. L. Simmons, K. Polzin, R. Pinkel, A. Pickering, N. J. Norton, J. D. Nash, R. Musgrave, L. M. Merchant, A. V. Melet, B. Mater, S. Legg, W. G. Large, E. Kunze, J. M. Klymak, M. Jochum, S. R. Jayne, R. W. Hallberg, S. M. Griffies, G. Danabasoglu, E. P. Chassignet, M. C. Buijsman, F. O. Bryan, B. P. Briegleb, A. Barna, B. K. Arbic, J. K. Ansong, and M. H. Alford. Climate process team on internal wave-driven ocean mixing. *Bulletin of the American Meteorological Society*, 98(11):2429–2454, 2017. doi: 10.1175/BAMS-D-16-0030.1.

G. Madec. NEMO ocean engine. *Note du Pôle de modélisation*, 2016. doi: 10.1016/j.joms.2014.06.438.

E. Maier-Reimer, K. Hasselmann, D. Olbers, and J. Willebrand. An ocean circulation model for climate studies, 1982. Max-Planck-Institut für Meteorologie. (Umweltforschungsplan des Bundesministers des Innern - Entwicklung von Klimamodellen; FB 104 02 612).

J. Marshall, A. Adcroft, C. Hill, L. Perelman, and C. Heisey. A finite-volume, incompressible navier stokes model for, studies of the ocean on parallel computers. *Journal of Geophysical Research C: Oceans*, 102(C3):5753–5766, 1997. doi: 10.1029/96JC02775.

J. C. McWilliams. Modeling the oceanic general circulation. *Annual Review of Fluid Mechanics*, 28:215–248, 1996. doi: 10.1146/annurev.fl.28.010196.001243.

P. Müller. *The equations of oceanic motions*. Cambridge University Press, 2006. doi: 10.1017/CBO9780511617843.

P. S. Peixoto and S. R. M. Barros. On vector field reconstructions for semi-Lagrangian transport methods on geodesic staggered grids. *Journal of Computational Physics*, 273:185–211, 2014. doi: 10.1016/j.jcp.2014.04.043.

M. R. Petersen. Residual potential energy, 2019. URL `https://github.com/MPAS-Dev/MPAS-QuickViz/tree/master/ocean/residual_potential_energy`. Last accessed: Aug. 31, 2020.

M. R. Petersen, D. W. Jacobsen, T. D. Ringler, M. W. Hecht, and M. E. Maltrud. Evaluation of the arbitrary Lagrangian-Eulerian vertical coordinate method in the MPAS-Ocean model. *Ocean Modelling*, 86:93–113, 2015. doi: 10.1016/j.ocemod.2014.12.004.

H.-O. Pörtner, D. Roberts, V. Masson-Delmotte, P. Zhai, M. Tignor, E. Poloczanska, K. Mintenbeck, A. Alegria, M. Nicolai, J. Okem, A. Petzold, B. Rama, and N. Weyer (eds). IPCC Special Report on the Ocean and Cryosphere in a Changing Climate. Technical report, In press., 2019.

T. Ringler, M. Petersen, R. L. Higdon, D. Jacobsen, P. W. Jones, and M. Maltrud. A multi-resolution approach to global ocean modeling. *Ocean Modelling*, 69:211–232, sep 2013. doi: 10.1016/J.OCEMOD.2013.04.010.

A. F. Shchepetkin and J. C. McWilliams. The regional oceanic modeling system (ROMS): a split-explicit, free-surface, topography-following-coordinate oceanic model. *Ocean Modelling*, 9(4):347–404, 2005. doi: 10.1016/J.OCEMOD.2004.08.002.

A. F. Shchepetkin and J. C. McWilliams. Computational Kernel Algorithms for Fine-Scale, Multiprocess, Longtime Oceanic Simulations. *Handbook of Numerical Analysis*, 14:121–183, 2009. doi: 10.1016/S1570-8659(08)01202-0.

Y. Soufflet, P. Marchesiello, F. Lemarié, J. Jouanno, X. Capet, L. Debreu, and R. Benshila. On effective resolution in ocean models. *Ocean Modelling*, 98:36–50, feb 2016. doi: 10.1016/J.OCEMOD.2015.12.004.

P. Spence, S. M. Griffies, M. H. England, A. M. C. Hogg, O. A. Saenko, and N. C. Jourdain. Rapid subsurface warming and circulation changes of Antarctic coastal waters by poleward shifting winds. *Geophysical Research Letters*, 41(13):4601–4610, 2014. doi: 10.1002/2014GL060613.

C. Vic, A. C. Garabato, J. A. Green, C. Spingys, A. Forryan, Z. Zhao, and J. Sharples. The lifecycle of semidiurnal internal tides over the Northern Mid-Atlantic Ridge. *Journal of Physical Oceanography*, 48(1):61–80, 2018. doi: 10.1175/JPO-D-17-0121.1.

H. Wan, M. A. Giorgetta, G. Zängl, M. Restelli, D. Majewski, L. Bonaventura, K. Fröhlich, D. Reinert, P. Rípodas, L. Kornblueh, and J. Förstner. The ICON-1.2 hydrostatic atmospheric dynamical core on triangular grids – Part 1: Formulation and performance of the baseline version. *Geoscientific Model Development*, 6:735–763, 2013. doi: 10.5194/gmd-6-735-2013.

M. Ward and Y. Zhang. Scalability of global 0.25° ocean simulations using MOM. *IFIP Advances in Information and Communication Technology*, 448:542–551, 2015. doi: 10.1007/978-3-319-15994-2_55.

K. B. Winters, P. N. Lombard, J. J. Riley, and E. A. D'Asaro. Available potential energy and mixing in density-stratified fluids. *Journal of Fluid Mechanics*, 289:115–128, 1995. doi: 10.1017/S002211209500125X.

P. J. Wolfram and O. B. Fringer. Mitigating horizontal divergence "checker-board" oscillations on unstructured triangular C-grids for nonlinear hydrostatic and non-hydrostatic flows. *Ocean Modelling*, 69:64–78, 2013. doi: 10.1016/j.ocemod.2013.05.007.

C. Wunsch and R. Ferrari. Vertical mixing, energy, and the general circulation of the oceans. *Annual Review of Fluid Mechanics*, 36(1):281–314, 2004. doi: 10.1146/annurev.fluid.36.050802.122121.

S. T. Zalesak. Fully multidimensional flux-corrected transport algorithms for fluids. *Journal of Computational Physics*, 31(3):335–362, 1979. doi: 10.1016/0021-9991(79)90051-2.

G. Zängl, D. Reinert, P. Rípodas, and M. Baldauf. The ICON (ICOsahedral Non-hydrostatic) modelling framework of DWD and MPI-M: Description of the non-hydrostatic dynamical core. *Quarterly Journal of the Royal Meteorological Society*, 141(687):563–579, 2015. doi: 10.1002/qj.2378.

Acknowledgments

First and foremost, I would like to thank my PhD supervisors and advisory panel chair: Peter Korn for his support and patience as well as Jochem Marotzke and Johanna Baehr for their guidance during the last years, which let me finish this thesis.

I like to thank Helmuth Haak and Leonidas Lindarkis for their help, whenever I had questions around the implementation of ICON-O.

I am very grateful to Mark R. Petersen and Siddhartha Bishnu, both from LANL, and Florian Lemarié from Inria Grenoble for discussions and ideas around time-stepping.

Special thanks belongs to the IMPRS-ESM office, Antje Weitz, Connie Kampmann and Michaela Born for their endless effort as well as to Kornelia Müller.

I am very thankful to family: my parents Hannah and Wolfgang, for all their support and wishes over the years; to Julian, Tina and Lea for more than amazing breakfasts; and Mirjam for all her energy and caring.

I want to thank Veit and Bernhard for being wonderful friends; Alex and Leo for joyful sessions; Mia and Caro for good coffee breaks; Bene, Daniel, Milaim and Liz for even more music; Charles, Nika, Hannah, Lotta, Hannah, Tobi for being amazing flat mates wherever I have been; and Hannah for being a caring friend. For being wonderful friends, time at Bayreuth and before, running, climbing, concerts and much more, I want to thank Manu, Flo, Anita, Stefan, Stefan, Maike, Theresa, Kristin, Kaddi and Anki. Clara, thank you for everything.

From the bottom of my heart, I want to thank everyone, from people closest to me to people that I occasionally meet, thank you for your love and kindness.

Versicherung an Eides statt

Declaration of oath

Hiermit versichere ich an Eides statt, dass ich die vorliegende Dissertation mit dem Titel: "*A split-explicit time-stepping scheme for ICON-Ocean*" selbstständig verfasst und keine anderen als die angegebenen Hilfsmittel – insbesondere keine im Quellenverzeichnis nicht benannten Internet-Quellen – benutzt habe. Alle Stellen, die wörtlich oder sinngemäß aus Veröffentlichungen entnommen wurden, sind als solche kenntlich gemacht. Ich versichere weiterhin, dass ich die Dissertation oder Teile davon vorher weder im In- noch im Ausland in einem anderen Prüfungsverfahren eingereicht habe und die eingereichte schriftliche Fassung der auf dem elektronischen Speichermedium entspricht.

Hamburg, den 13.10.2020

Lukas Krönert

Hinweis / Reference

Die gesamten Veröffentlichungen in der Publikationsreihe des MPI-M
„Berichte zur Erdsystemforschung / Reports on Earth System Science“,
ISSN 1614-1199

sind über die Internetseiten des Max-Planck-Instituts für Meteorologie erhältlich:
http://www.mpimet.mpg.de/wissenschaft/publikationen.html

All the publications in the series of the MPI -M
„Berichte zur Erdsystemforschung / Reports on Earth System Science“,
ISSN 1614-1199

are available on the website of the Max Planck Institute for Meteorology:
http://www.mpimet.mpg.de/wissenschaft/publikationen.html